Available online at www.sciencedirect.com

jmr&t Journal of Materials Research and Technology

journal homepage: www.elsevier.com/locate/jmrt

Original Article

Effects of Ce–Dy rare earths co-doping on various features of Ni–Co spinel ferrite microspheres prepared via hydrothermal approach

M.A. Almessiere [a,b,*], B. Unal [c], Y. Slimani [b], H. Gungunes [d], M.S. Toprak [e], N. Tashkandi [f], A. Baykal [f], M. Sertkol [g], A.V. Trukhanov [h,i,j], A. Yıldız [k], A. Manikandan [l,m]

[a] Department of Physics, College of Science, Imam Abdulrahman Bin Faisal University, P.O. Box 1982, Dammam, 31441, Saudi Arabia
[b] Department of Biophysics, Institute for Research and Medical Consultations (IRMC), Imam Abdulrahman Bin Faisal University, P.O. Box 1982, Dammam, 31441, Saudi Arabia
[c] Institute of Forensic Sciences & Legal Medicine, Istanbul University–Cerrahpaşa, Buyukcekmece Campus, Buyukcekmece, Istanbul, 34500, Turkey
[d] Department of Physics, Hitit University, Çevre Yolu Bulvarı, Çorum, 19030, Turkey
[e] Department of Applied Physics, KTH-Royal Institute of Technology, Stockholm, SE10691, Sweden
[f] Department of Nanomedicine Research, Institute for Research and Medical Consultations (IRMC), Imam Abdulrahman Bin Faisal University, P.O. Box 1982, Dammam, 31441, Saudi Arabia
[g] Department of Basic Science, Deanship of Preparatory Year and Supporting Studies, Imam Abdulrahman Bin Faisal University, P.O. Box 1982, Dammam, 34212, Saudi Arabia
[h] Scientific-Practical Materials Research Centre of NAS of Belarus, P. Brovki Str., 19, Minsk, 220072, Belarus
[i] South Ural State University, Lenin Av., 76, Chelyabinsk, 454080, Russia
[j] L.N. Gumilyov Eurasian National University, 2, Satpayev Str., Nur-Sultan, 010000, Kazakhstan
[k] Namik Kemal University, Çorlu Engineering Faculty, Textile Engineering Department, Çorlu-Tekirdag, 59860, Turkey
[l] Department of Chemistry, Bharath Institute of Higher Education and Research (BIHER), Bharath University, Chennai, Tamil Nadu, 600 073, India
[m] Center for Catalysis and Renewable Energy, Bharath institute of Higher Education and Research (BIHER), Chennai, Tamil Nadu, 600 073, India

ARTICLE INFO

Article history:
Received 18 May 2021
Accepted 28 July 2021
Available online 3 August 2021

Keywords:
NiCo spinel ferrites
Ferrite microsphere

ABSTRACT

The effects of Ce–Dy co-doping on the crystal structure, optical, dielectric, magnetic properties, and hyperfine interactions of Ni–Co spinel ferrite microspheres synthesized hydrothermally have been studied. A series of ferrites with the general formula $Ni_{0.5}Co_{0.5}Ce_xDy_xFe_{2-2x}O_4$ were synthesized with x values ranging from 0.00 to 0.10. The phase, crystallinity, and morphology of ferrite microspheres were analyzed by X-ray powder diffractometry (XRD), scanning and transmission electron microscopes (SEM and TEM), respectively. The structural analyses of the synthesized ferrite microspheres confirmed their high purity and cubic crystalline phase. The Diffuse reflectance spectroscopic (DRS)

* Corresponding author.
E-mail address: malmessiere@iau.edu.sa (M.A. Almessiere).
https://doi.org/10.1016/j.jmrt.2021.07.142

Dielectric properties
Conductivity
Hyperfine interaction
Ferrimagnetic

measurements were presented to calculate direct optical energy band gaps (E_g) and is found in the range 1.63 eV - 1.84 eV. ^{57}Fe Mossbauer spectroscopy showed that the hyperfine magnetic field of tetrahedral (A) and octahedral (B) sites decreased with the substitution of Dy^{3+}-Ce^{3+} ions that preferentially occupy the B site. The impact of the rare-earth content (x) on the magnetic features of the prepared NiCo ferrite microspheres was investigated by analyzing M-H loops, which showed soft ferrimagnetism. The magnetic features illustrate a great impact of the incorporation of Ce^{3+}-Dy^{3+} ions within the NiCo ferrite structure. The saturation magnetization (M_s), remanence (M_r), and coercivity (H_c) increased gradually with increasing Ce–Dy content. At $x = 0.04$, M_s, M_r, and H_c attain maximum values of about 31.2 emu/g, 11.5 emu/g, and 512.4 Oe, respectively. The Bohr magneton (n_B) and magneto-crystalline anisotropy constant (K_{eff}) were also determined and evaluated with correlation to other magnetic parameters. Further increase in Ce^{3+}-Dy^{3+} content (i.e., $x \geq 0.06$) was found to decrease M_s, M_r, and H_c values. The variations in magnetic parameters (M_s, M_r, and H_c) were largely caused by the surface spins effect, the variations in crystallite/particle size, the distribution of magnetic ions into the different sublattices, the evolutions of magneto-crystalline anisotropy, and the variations in the magnetic moment (n_B). The squareness ratios were found to be lower than the predicted theoretical value of 0.5 for various samples, indicating that the prepared Ce–Dy substituted NiCo ferrite microspheres are composed of NPs with single-magnetic domain (SMD). Temperature and frequency-dependent electrical and dielectric measurements have been done to estimate the ac/dc conductivity, dielectric constant, and tangent loss values for all the samples. The ac conductivity measurements confirmed the power-law rules, largely dependent on Ce–Dy content. Impedance analysis stated that the conduction mechanisms in all samples are mainly due to the grains-grain boundaries. The dielectric constant of NiCo ferrite microspheres give rise to normal dielectric distribution, with the frequency depending strongly on the Ce–Dy content. The observed variation in tangential loss with frequency can be attributed to the conduction mechanism in ferrites, like Koop's phenomenological model.

1. Introduction

Spinel ferrites are metal oxides with spinel structure of [(M^{2+})(Fe_2^{3+})O_4] and crystallize in the FCC (face-centered cubic structure). According to the distribution of the M^{2+} (divalent) and Fe^{3+} (trivalent) ions between the tetrahedral (T_d) and octahedral (O_h) cation sites, they are categorized as normal or inverse spinel ferrites [1,2]. The metal cations at both sites are tetrahedrally and octahedrally coordinated to oxygen atoms, respectively [2]. Spinel ferrites are a very important class of compounds due to their technological usage (from biomedical to industrial), but their physicochemical properties are highly dependent on the types, amounts, and positions of the metal cations in the crystallographic structure [3]. The most used spinel ferrites are Fe_3O_4, Co_3O_4, $CoFe_2O_4$, $CuFe_2O_4$, $MnFe_2O_4$, $NiFe_2O_4$ and $ZnFe_2O_4$. The major applications of spinel ferrites include cancer diagnosis, cancer gene therapy and drug delivery [4], catalyst and pollutant removal via adsorption or photodegradation [5], as gas sensor [6], in high-frequency devices [7], water splitting [8], membrane modification [9], and hyperthermia [10]. They are also being used in microwave (MW) devices, biotechnology, high-speed digital recording, ferrofluids, magnetic disks for recording and refrigeration [11]. Recently, rare earth ions substituted spinel ferrites have emerged as a promising strategy to improve their physical properties [12].

The physical properties of spinel ferrites also depend upon the synthesis techniques. They can be synthesized by several chemical synthesis techniques such as co-precipitation, hydrothermal, solvothermal, microemulsion, sol-gel auto-combustion methods, etc. [13]. Among these spinel ferrites, Co–Ni ferrites, due to the excellent electromagnetic properties, Co–Ni ferrites are suitable for application in high-frequency devices (such as read/write heads for high-speed digital tape, transformer cores, high-quality filters, rod antenna radio frequency circuits, and operating devices) [14–16]. Apart from the spinel ferrites, hollow spinel ferrite microspheres (SFMSs) have also a special importance due to their intrinsic properties (low density, high surface area, special optical property, high packing, larger specific surface area, hollow structure, and nanostructured wall, etc.). According to these properties, ferrite spheres with a hollow structure are expected to have advantages over their solid counterparts. They have a wide-range of application in chemistry, biotechnology, materials science, catalysis, controlled release of drugs, lithium-ion batteries, chemical sensors, optical materials, photocatalysis, and photoluminescent materials, etc. [18–23]. Various synthesis methods such as spraying, dripping, emulsion, and aerosol-assisted self-assembly, hydrothermal/

Table 1 – The number of moles of each element used during the synthesis of SFMSs.

x	Ni	Co	Ce	Dy	Fe
0.00	0.5	0.5	–	–	2
0.02	0.5	0.5	0.02	0.02	1.96
0.04	0.5	0.5	0.04	0.04	1.92
0.06	0.5	0.5	0.06	0.06	1.88
0.08	0.5	0.5	0.08	0.08	1.84
0.10	0.5	0.5	0.1	0.1	1.80

solvothermal, gas-phase diffusion, and template [24–26] methods are being currently used for the fabrication of carbon SFMSs. Among them, the solvothermal/hydrothermal approach is an efficient and economic route for the fabrication of monodispersed hollow ferrites.

In this study, we used the carbon spheres as templates for the preparation of hollow SFMSs of $Ni_{0.5}Co_{0.5}Ce_xDy_xFe_{2-2x}O_4$ ($x \leq 0.10$). The effects of sample composition, structure and morphology on the magnetic and dielectric properties and hyperfine interactions were investigated.

2. Experimental

2.1. Preparation procedure for the carbon template

The carbon template was prepared by melting 1M of glucose in deionized (DI) water at 40 °C. Then, it was inserted into a Teflon-lined autoclave and heated in an oven at 180 °C for 10h. After filtration and several washing steps, solid products were dried at 80 °C in an oven.

2.2. Synthesis of $Ni_{0.5}Co_{0.5}Ce_xDy_xFe_{2-2x}O_4$ carbon SFMSs

The $Ni_{0.5}Co_{0.5}Ce_xDy_xFe_{2-2x}O_4$ ($0.00 \leq x \leq 0.10$) SFMSs were synthesized using a hydrothermal approach. Specific weights of $Ni(NO_3)_2.6(H_2O)$, $Fe(NO_3)_3.9(H_2O)$, $Co(NO_3)_2.6H_2O$, $Dy(NO_3)_3.6(H_2O)$ and $Ce(NO_3)_3.6(H_2O)$ as listed in Table 1, where 1g of carbon microspheres were thawed in 200 mL of DI water under continuous stirring for 30 min. The pH of the solution was adjusted to neutral by adding some drops of ammonia solution. The solution was exposed to sonication for 30 min. After that, the mixture was put in the autoclave (Teflon lined) at 180 °C for 10 h. Eventually, the solution was dried, ground, and placed in a furnace at 500 °C for 4h.

2.3. Characterization

The structure analysis was accomplished by X-ray diffractometer (Rigaku Benchtop Miniflex, Cu Kα radiation). The surface analysis of the samples was performed by scanning electron microscopy (SEM, FEI Titan ST with EDX) and transmission electron microscopy (TEM, FEI Morgagni 268). The percent diffuse reflectance UV–Vis spectrophotometry has been used to study the optical properties of samples and determine the band structure. The dielectric measurements were achieved via the Novocontrol Alpha impedance analyzer (Temperature ranging between 20 and 120 °C and frequency ranging between 1 Hz and 3.0 MHz). The films were sandwiched between gold blocking electrodes and the conductivities were measured in the frequency range 0.1 Hz–1 MHz at 10 °C intervals. POLON spectrometer configured in a vertical geometry and operating in a constant acceleration mode equipped with $^{57}Co(Rh)$ radioactive source was used for measurements. The magnetic properties were evaluated using a quantum design PPMS coupled with a vibrating sample magnetometer (VSM) head.

3. Results & discussion

3.1. Phase characterization

Fig. 1a and b represent the structure of $Ni_{0.5}Co_{0.5}Ce_xDy_xFe_{2-2x}O_4$ ($x = 0.02$) SFMSs and XRD powder patterns of carbon microsphere and $Ni_{0.5}Co_{0.5}Ce_xDy_xFe_{2-2x}O_4$ ($x \leq 0.10$) SFMSs, respectively. Fig. 1a showed a pattern with a single and broad peak at 20°, which is assigned to the (002) plane of carbon. The unit cell of $Ni_{0.5}Co_{0.5}Ce_xDy_xFe_{2-2x}O_4$ is presented in Fig. 1b. Fig. 1c exhibited the typical peaks of Ni–Co SFMSs with the absence of any impurities in all SFMSs compositions, which indicated that the compositions were pure nickel-cobalt spinel ferrite. The diffraction peaks and relative intensities of all patterns match well with the standard data for cubic spinel ferrite reported in (ICDD card no 96-591-0065). It is obvious that the most intense peak (311) is broadened, which indicated the smaller crystallites size. The experimental XRD data were refined using Match3! and Full proof program to calculate the cell parameters and cell volume (Table 2) [27]. The average values of crystallites size (D_{XRD}) were calculated by means of the Debye-Scherer formula by taking into consideration the most intense peak (311). D_{XRD} values are found to be in 6–9 nm range. In the present case, the ionic radii of Dy^{3+} (1.02 Å) and Ce^{3+} (1.14 Å) are larger than Fe^{3+} (0.67 Å) ion, and hence a small increase in the lattice parameters for $Ni_{0.5}Co_{0.5}Ce_xDy_xFe_{2-2x}O_4$ ($0.00 < x \leq 0.10$) SFMSs has been observed. The lattice constant, 'a_o', is higher for all substitutions than the host NiCo spinel ferrite ($x = 0.0$). Although the introduction of large rare-earth (RE^{3+}) ions into the spinel structure of NiCo spinel ferrite leads to a distortion of tetrahedral and octahedral symmetry, tending to the creation of iron vacancies, which further could decrease the lattice parameter. But the degree of decrease is different for each composition.

3.2. Morphological analysis

SEM micrographs of $Ni_{0.5}Co_{0.5}Ce_xDy_xFe_{2-2x}O_4$ ($x = 0.02$ and 0.06) SFMSs are presented in Fig. 2. Figs. 3 and 4 shows the TEM micrographs of $Ni_{0.5}Co_{0.5}Ce_xDy_xFe_{2-2x}O_4$ ($x = 0.02$) SFMSs. All samples revealed spherical morphology with a low degree of agglomeration, and typical micrographs observed are

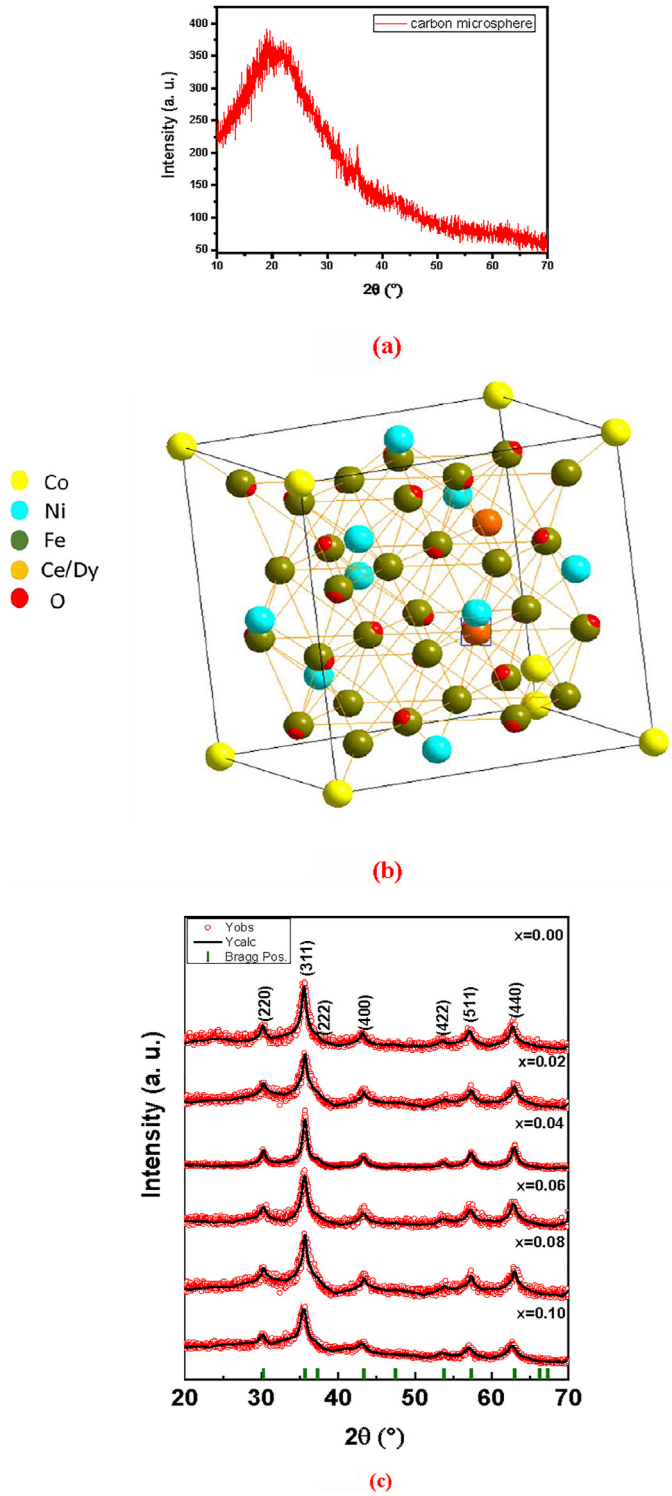

Fig. 1 – (a) XRD patterns of carbon microsphere, (b) the cubic unit cell of $Ni_{0.5}Co_{0.5}Ce_xDy_xFe_{2-2x}O_4$ SFMSs, and (c) XRD patterns of $Ni_{0.5}Co_{0.5}Ce_xDy_xFe_{2-2x}O_4$ ($x \leq 0.10$) SFMSs.

represented by the samples with x = 0.02 and 0.06. The micrographs revealed the presence of smooth, uniform, spherical particles with an average size of around 10 nm. The elemental composition was verified through EDX, as the weight percentage of the constituent elements as Ni, Co, Ce, Dy, O, C and Fe could be extracted from the EDX spectra. Elemental maps of $Ni_{0.5}Co_{0.5}Ce_xDy_xFe_{2-2x}O_4$ (x = 0.02) SFMSs, as representative of the materials series, ferrite microspheres are shown in Fig. 2. In Figs. 3 and 4, a high magnification TEM micrograph and a selected area electron diffraction (SAED) pattern are presented. Some of the observed planes are indicated on the micrograph, with measured d-spacings of about 1.5 nm and 0.7 nm, indexed to (4 4 0) and (11 1 1) Bragg diffractions of spinel ferrites (ICDD card no 96-591-0065). SAED

pattern shows distinctive diffraction spots forming ring patterns, which is indicative of the polycrystalline character of the sample. The observed rings are indexed to the same crystal structure as the XRD patterns revealed (ICDD card no 96-591-0065).

3.3. Optical properties

The optical properties of $Ni_{0.5}Co_{0.5}Ce_xDy_xFe_{2-2x}O_4$ ($x \leq 0.10$) SFMSs were explored by analyzing the UV–Vis diffuse reflectance (%DR) spectra. Fig. 5 represented the UV–vis spectra of $Ni_{0.5}Co_{0.5}Ce_xDy_xFe_{2-2x}O_4$ ($x \leq 0.10$) SFMSs. All %DR spectra were recorded in the wavelength range from 200 to 900 nm. The reflectance intensities of all compositions are between 15.20% and 60%. Above 650 nm, the reflection significantly rises with different ratios.

The optical band gap (E_g) was calculated via Kubelka and Munk (K-M) theory by using the diffuse reflectance spectra as follows [28,29]:

$$\frac{K}{S} = \frac{(1-R_\infty)^2}{2R_\infty} \equiv F(R_\infty) \quad (1)$$

where R is reflectance and dependent on K-M function, $F(R_\infty)$ is identified as the ratio between absorption coefficient K and scattering coefficient S, the ∞ symbol indicates the thick enough layer created by nanocrystals in the sample holder of the spectrophotometer. The influence of substitution with various ratios of Dy^{3+} and Ce^{3+} on energy band gaps was estimated by the Tauc formula [30–32]:

$$(F(R_\infty).h\upsilon)^n = A(h\upsilon - E_g) \quad (2)$$

whereas h is the Plank's constant, υ is the light frequency, A is the proportionality constant, exponent n defines a direct allowed electronic transition with the magnitude of 2. The E_g values for all ratios were computed by plotting $(F(R_\infty)h\upsilon)^2$ versus energy $(h\upsilon)$. The intersection of the tangent line with the linear part of the plotted curve will immediately yield E_g in units of eV. The pure mixed spinel $Ni_{0.5}Co_{0.5}Fe_2O_4$ SFMSs has a minimum E_g value of 1.63 eV. All substituted samples have higher bandgap magnitudes as follow 1.65, 1.77, 1.79, 1.81 and 1.84 eV corresponding and increasing bandgap with increasing Dy^{3+}-Ce^{3+} ions concentration from $x = 0.02$ to $x = 0.10$. Accordingly, substitution with Dy^{3+} and Ce^{3+} ions influenced the direct E_g magnitude in comparison with $Ni_{0.5}Co_{0.5}Fe_2O_4$ SFMSs significantly, which refers to many factors such as creating an energy level, interface defects into the structure, crystallite size, and presence of trace impurities by substitution ions [33]. These results are caused by the synergistic influence of nano-ferrite with Dy^{3+}-Ce^{3+} ions that lead to a decrease in the electron-hole recombination and increase the Eg value [33].

Table 2 – Refined structural parameters for $Ni_{0.5}Co_{0.5}Ce_xDy_xFe_{2-2x}O_4$ ($x \leq 0.10$) SFMSs.

x	a (Å)	V (Å^3)	D_{XRD} (nm) ±0.05	χ^2 (chi^2)	R_{Bragg}
0.00	8.3611	584.50	6.8	1.30	16.0
0.02	8.4225	597.46	6.9	1.00	12.6
0.04	8.3625	584.80	9.1	1.10	11.1
0.06	8.3649	585.30	6.3	1.40	15.8
0.08	8.3668	585.71	5.4	1.35	13.0
0.10	8.3885	590.27	6.7	0.9	15.0

3.4. Mossbauer study

Mossbauer spectra and parameters of $Ni_{0.5}Co_{0.5}Ce_xDy_xFe_{2-2x}O_4$ ($x \leq 0.10$) SFMSs at room temperature (RT) are presented in Fig. 6 and Table 3, respectively. The spectra were fitted by using the superposition of two or more magnetic sextets and one non-magnetic doublet. The largest hyperfine with a greater isomer shift is attributed to Fe^{3+} cations located at Oh (B-site), whereas the lower values correspond to Fe^{3+} cations in Td (A-site). It is well known that the Fe^{3+} located in A site is surrounded by 12 B site Fe^{3+} ions, whereas the Fe^{3+} located in B site is surrounded by 6 A site Fe^{3+} ions. Therefore, the number of sextets at B sites in ferrite system may increases until six sextets because of the close neighbor coordination of A site around B site is nearer in comparison to B sites around A sites [34].

As seen in Fig. 7, while the isomer shift of B site exhibits an increasing trend, that of A site almost remains invariant with the increasing concentration of doping ions [35]. The increase of Isomer shift values of B site with substitution suggested that the s electron density of Fe^{3+} ions at the B site decrease with substitution. This indicates that the cubic symmetry of O^{2-} surrounding Fe^{3+} ions is not altered upon doping. As seen in Fig. 7, the relative area of B site decreases with the increase of Dy^{3+}-Ce^{3+} concentration. The area of sextets and doublet is directly proportional to the amount of Fe^{3+} ions in the corresponding sites. These results show the larger ions of Dy^{3+} (1.02 Å) and Ce^{3+} (1.14 Å) prefer to occupy B site, because there is not enough space in the A site. Due to the large ionic radii of rare-earth ions, they generally prefer the octahedral B site [36]. At the same time, the hyperfine magnetic fields of A and B sites are decreasing with increasing doped ions are given in Fig. 6. The displacement of higher magnetic moment with Dy^{3+} (10.5 μ_B) and low magnetic moment Ce^{3+} (2.5 μ_B) ions by Fe^{3+} (5 μ_B) ions on B sites results in a decrease in the magnetic moment on the B site. This displacement reduced the average number of magnetic bonds of $Fe_A^{3+} - O - Fe_B^{3+}$ and consequently, Fe^{3+} nuclei experience a reduction in the magnetic field at both sublattices. Therefore, the hyperfine magnetic field of A and B sites decreased with substitutions. Similar trend was observed in Ce and Dy doped cobalt ferrites [37].

3.5. Electrical & dielectric properties

3.5.1. AC conductivity

Besides the performance of charge carriers in an alternating electric field, the conduction and mobility charging mechanism become clear with the ac conductivity study. Therefore, the conduction and mobility charge mechanism in a variable electric field can be interpreted in more detail with the study of ac conductivity. The ac conductivity of all ferrites can be evaluated by the following equation.

$$\sigma_{ac} = \omega\varepsilon_0\varepsilon' tan\delta \quad (3)$$

where $\varepsilon'$is the relative permittivity, ε_0 is the absolute

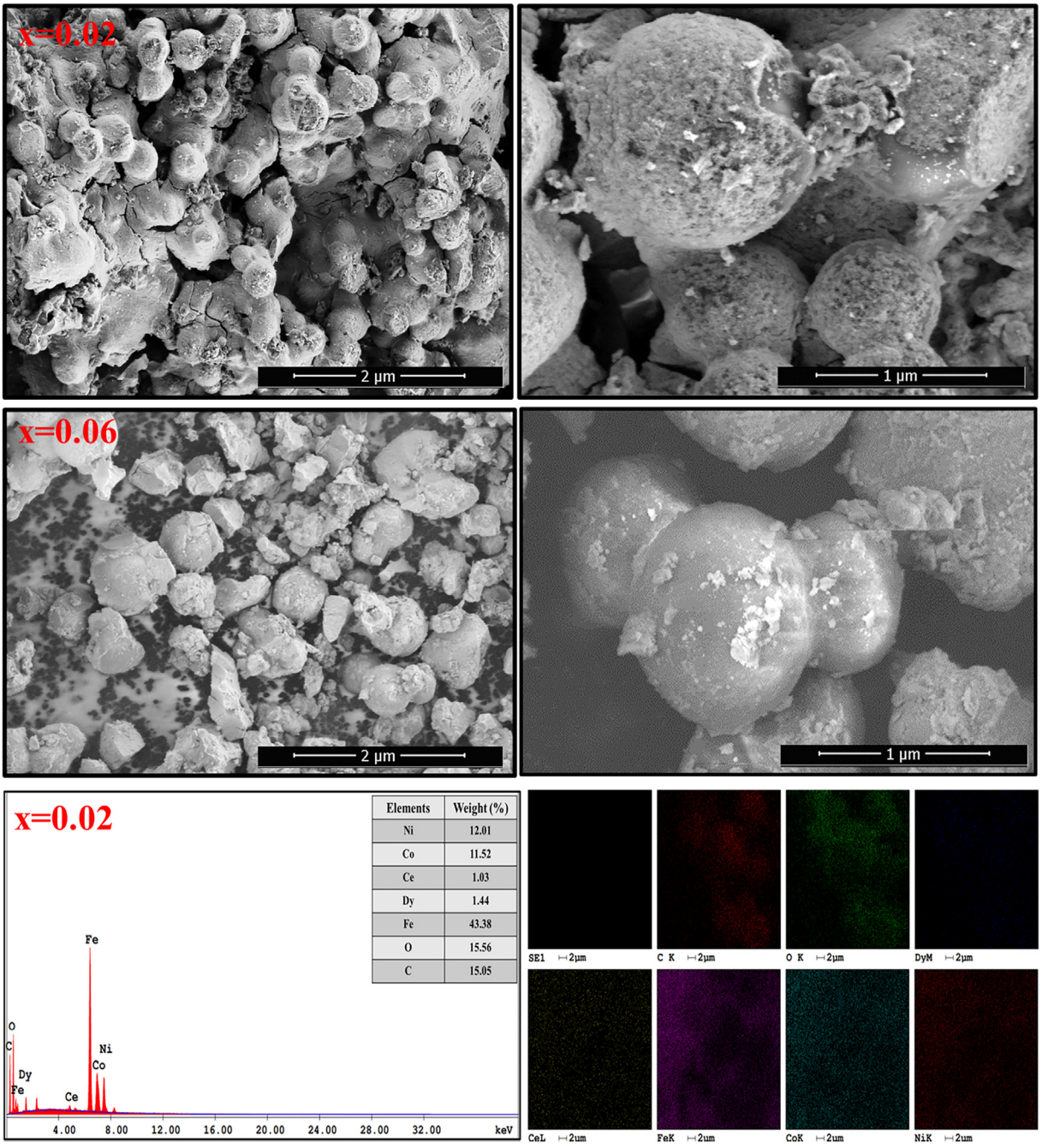

Fig. 2 – SEM micrographs (x = 0.02, 0.06), EDX spectrum (x = 0.02) and elemental mapping of (x = 0.02) of $Ni_{0.5}Co_{0.5}Ce_xDy_xFe_{2-2x}O_4$ SFMSs.

permittivity, ω is the angular frequency of the applied electric field and $tan\delta$ is the tangent loss.

Characteristic ac conductivity of $Ni_{0.5}Co_{0.5}Ce_xDy_xFe_{2-2x}O_4$ ($x \leq 0.10$) SFMSs is shown in Fig. 8 as functions of both the temperature between 20 and 120 °C and frequency ranging from 1 Hz to 3.0 MHz. It is clear from the figure that the ac conductivity in the reference NiCo ferrite increases with frequency for all temperatures but remains constant with the temperature at lower frequencies, while increasing with the temperature at high frequency. Accordingly, the ac conductivity of all ferrite compounds increases with frequency, as is the usual behavior of ferrites. It is also obvious to see that ac conductivity fluctuates with increasing "x" in NiCo SFMSs. Analogous trends are observed in ac conductivity in NiCd and Li ferrites, both substituted with Co ions, since the ac conductivity is proportional to the loss tangent and dielectric constant [38]. Subsequently, the frequency-dependent trends in all conductivity curves are similar with some minor differences, e.g., x = 0.00, like 0.02; x = 0.04 is inversely like 0.10 and x = 0.06 is like 0.08. All ferrites increase with increasing

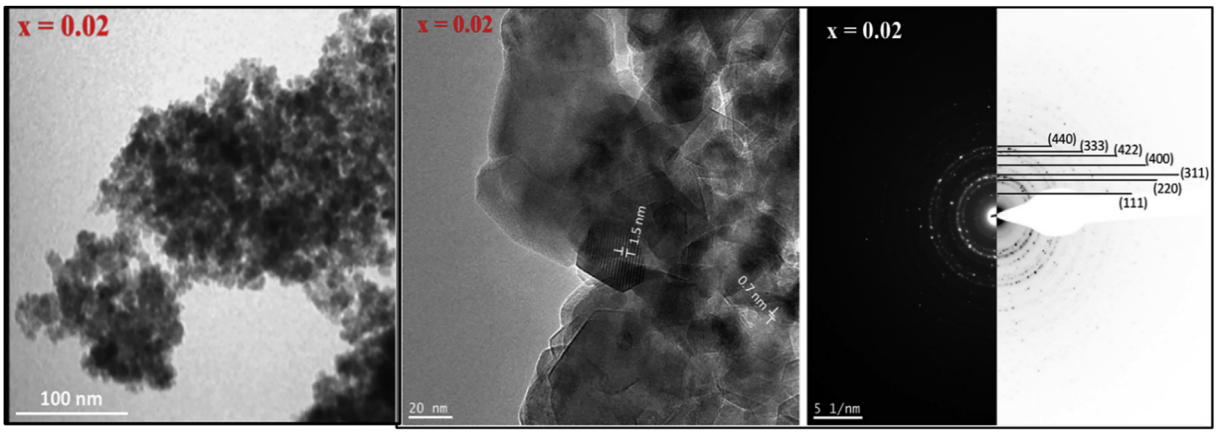

Fig. 3 – TEM micrographs of $Ni_{0.5}Co_{0.5}Ce_xDy_xFe_{2-2x}O_4$ (x = 0.02) SFMSs. Typical selected area electron diffraction (SAED) pattern, indexed to ICDD card no 96-591-0065.

frequency and process a power base law trend. For Ce–Dy ions substituted NiCo SFMSs at the ratios of x = 0.02, 0.06, and 0.08, identical trends occur along with the frequency variation while slight fluctuation exists at low frequencies especially for x = 0.02. For x = 0.04 and 0.10, ac conductivity represents a deep valley and a softer peak in the temperature transition region, respectively. Temperature dependency in conductivity for the reference NiCo ferrite remains constant at higher frequencies while it increases at the lower frequencies. For the co-substituted NiCo ferrites of x = 0.04 and 0.10 conductivity fluctuates along with the temperature variation for almost the whole interval of frequency, while those for x = 0.06 and 0.08 conductivity increase with the elevated temperature at lower frequency and fluctuates with the temperature at medium frequencies; endures constant at higher frequencies. It is interesting to deduce that concentration ("x") of Ce^{3+}-Dy^{3+} ions have some strong localized effect on the conduction mechanism in NiCo ferrites. Conductive grains become more active when the frequency rises due to the increase of hopping of electrons among ferric and ferrous ions. Thus, as the frequency increases, the conductivity increases. The conduction in ferrites is attributable to the exchange of electrons among ferrous and ferric ions. So, the *ac* conductivity performances of NiCo SFMSs could be pronounced based on Maxwell-Wagner dielectrics model [39].

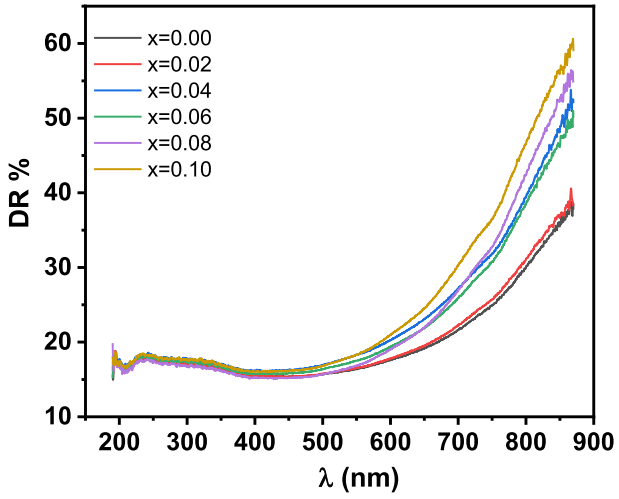

Fig. 4 – %DR spectra of $Ni_{0.5}Co_{0.5}Ce_xDy_xFe_{2-2x}O_4$ (x ≤ 0.10) SFMSs.

3.5.2. *DC conductivity*

The dc conductivity of $Ni_{0.5}Co_{0.5}Ce_xDy_xFe_{2-2x}O_4$ (x ≤ 0.10) SFMSs is shown in Fig. 9 in the form of Arrhenius plots. At low temperature dc conductivity increases with co-substitution ratios in NiCo ferrites while in transition region of 50–70 °C, it decreases with reciprocal thermal energy of $(k_BT)^{-1}$ for co-substitution ratios of x = 0.00, 0.06 and 0.08, and increments for x = 0.02, 0.04 and 0.10. In addition, at high temperature all decreases with the variation of $(k_BT)^{-1}$ except x = 0.10. It is clear that DC conductivity is greatly dependent on both temperature and co-substitution ratios. The presence of rare-earth ions in NiCo ferrite leads to a semiconductor behavior that shows the conductivity performance of NiCo ferrites by combining important Ce and Dy ions.

3.5.3. *Dielectric constant*

The characteristic dielectric constants of $Ni_{0.5}Co_{0.5}Ce_xDy_xFe_{2-2x}O_4$ (x ≤ 0.10) SFMSs are shown in Fig. 10 as functions of both temperature between 20 and 120 °C and frequency up to 3.0 MHz. The dielectric constant in NiCo ferrite declines with the rise in frequency for all temperatures, then slightly increases with the increase in temperature at lower frequencies. For NiCo ferrites co-substituted with Ce and Dy ions where x = 0.04, the constant decreases with increase in temperature while almost remaining constant along with the temperature ranges at x=0.02. Tendencies in dielectric constant curves for x=0.06 along temperatures ranging up to 120 °C seem to be like those for x=0.02, and being as narrow-flat changes for x=0.08. For the x = 0.10 NiCo SFMSs, it was observed that the temperature change in the x = 0.04 sample was in the opposite direction. Generally, some fluctuations occur along with the frequency and temperature variation. These dielectric responses of NiCo SFMSs are normal behavior in comparison with previous reports [40]. With x = 0.10, Ce and Dy ions

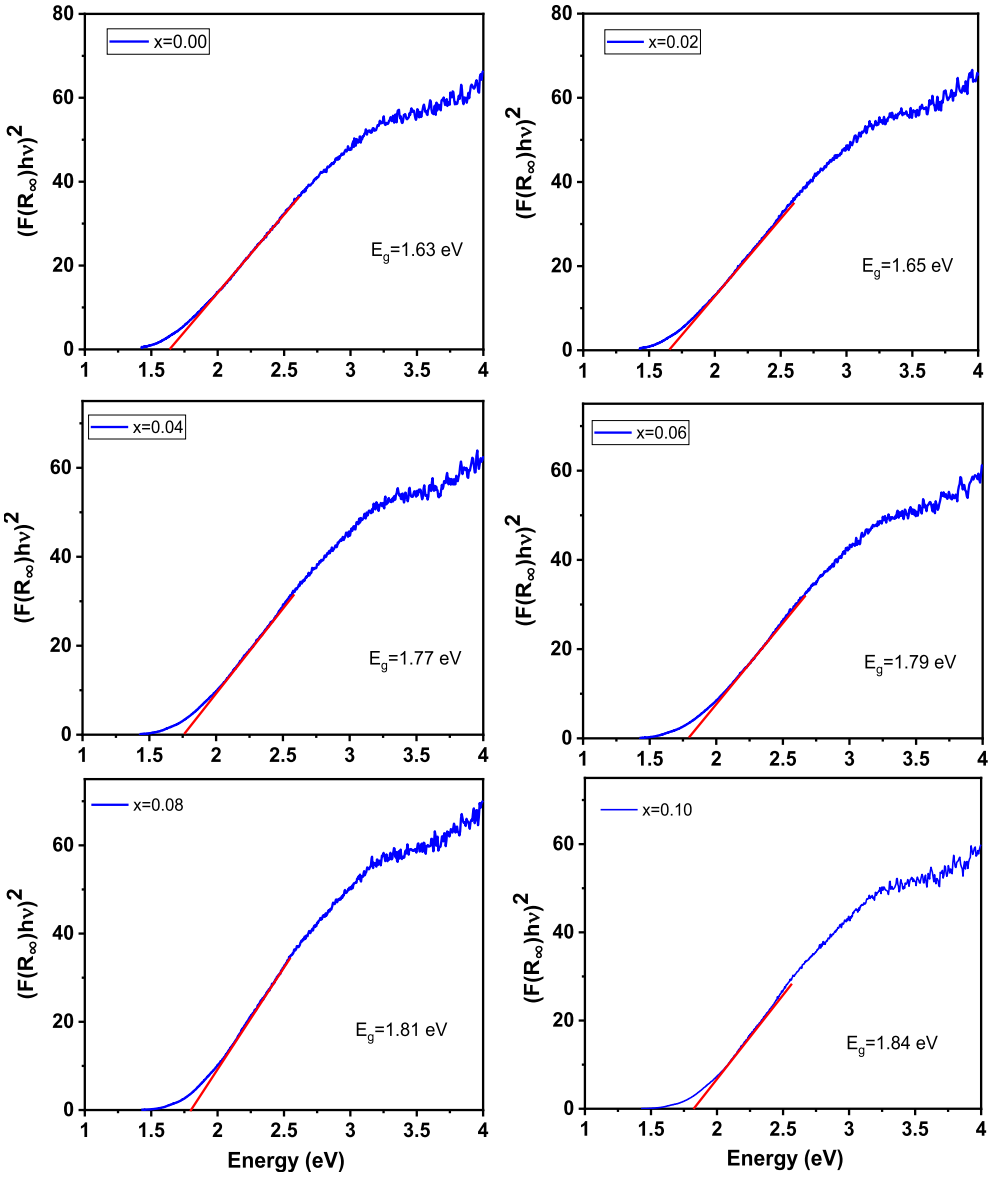

Fig. 5 – Tauc plots and estimated energy band gaps of $Ni_{0.5}Co_{0.5}Ce_xDy_xFe_{2-2x}O_4$ ($x \leq 0.10$) SFMSs.

substituted NiCo SFMSs show maximum dispersion due to the excess of ferrous ions.

At lower frequency, all NiCo SFMSs dissipate, which can be attributed to the space charge polarization. In accordance with the two-layer model of Maxwell-Wagner and Koop's phenomenological theory [41], the highly conductive grain at the insulating grains boundaries is responsible for the space charge polarization. Therefore, grain boundaries are more dominant than grains at lower frequencies. The dielectric constant is directly related to the size of the grain boundaries, while at higher frequencies it is frequency independent. This is because the exchange charge carriers among ferric and ferrous ions in Oh sites cannot follow the electric field if it exceeds a certain value. The electronic exchange among ferric and ferrous ions accomplishes the electric polarization behavior of NiCo ferrites if the dielectric constant decreases with frequencies. Also, the co-substituted Ce and Dy ions both occupy octahedral sites due to their large ion radii, reducing the amount of Fe ions. So, the transfer of electrons among ferric and ferrous ions is inhibited, leading to reduced polarization and hence results in their low values [42].

3.5.4. *Dielectric loss*

Characteristic dielectric loss of $Ni_{0.5}Co_{0.5}Ce_xDy_xFe_{2-2x}O_4$ ($x \leq 0.10$) SFMSs is shown in Fig. 11. It is clear from the figures that the dielectric loss in NiCo ferrite decreases with frequency for all temperatures but increases with temperature at lower frequencies. For Ce–Dy substituted NiCo ferrites of $x = 0.02$, 0.06, and 0.08 peaks and valleys occur along with the frequency variation while some fluctuation exists at low frequencies especially for $x = 0.02$. For $x = 0.04$ and 0.01. The dielectric loss represents a deep valley and a sharp peak in the temperature transition region, respectively.

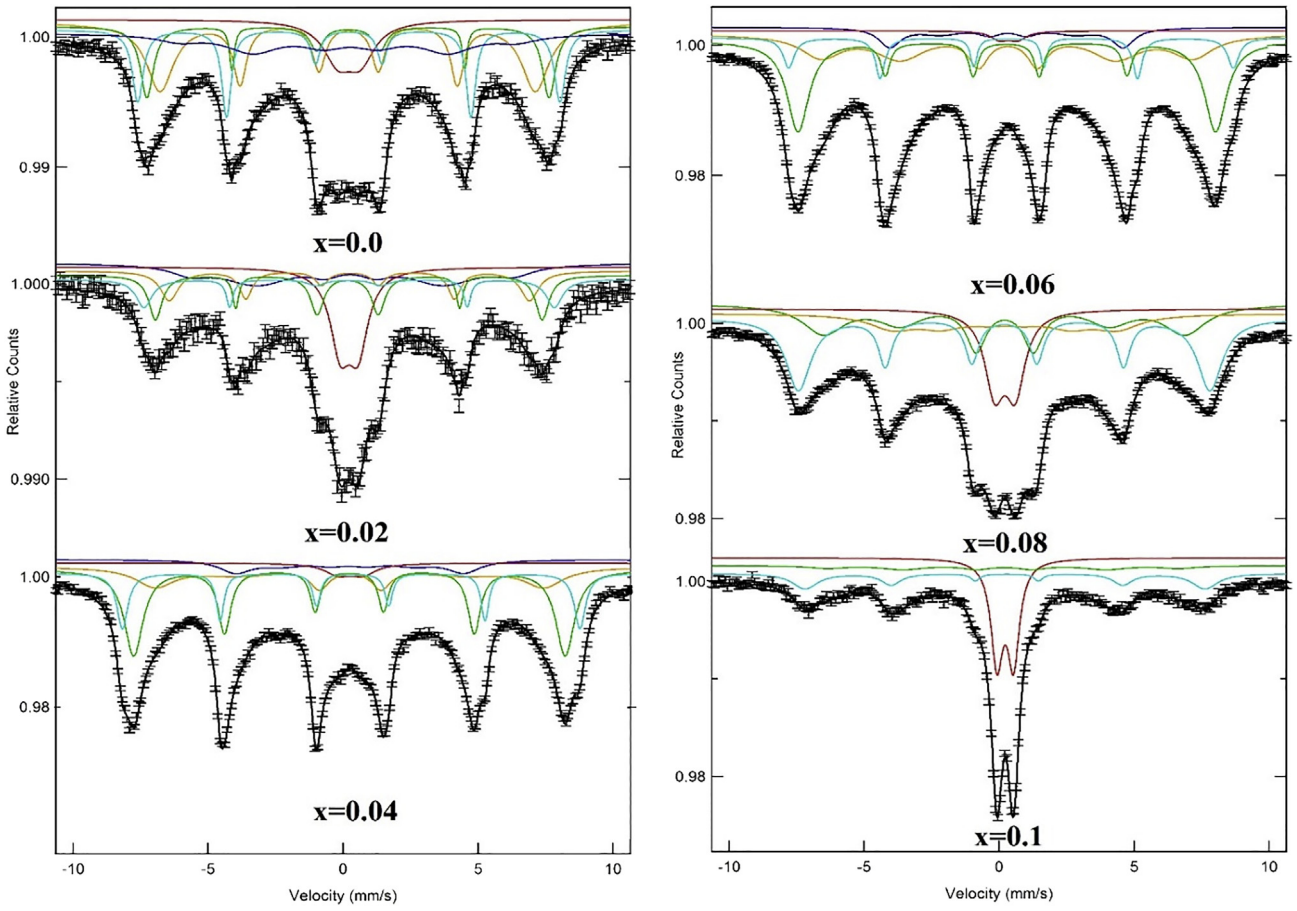

Fig. 6 – Mossbauer spectra of $Ni_{0.5}Co_{0.5}Ce_xDy_xFe_{2-2x}O_4$ ($x \leq 0.10$) SFMSs at RT.

3.5.5. *Dielectric loss tangent*

Characteristic dielectric tangent loss of $Ni_{0.5}Co_{0.5}Ce_xDy_xFe_{2-2x}O_4$ ($x \leq 0.1$) SFMSs is presented in Fig. 12. Identical to the dielectric loss, the loss tangent in NiCo ferrite reference decreases with frequency for all temperatures but increases with temperature at lower frequencies. For NiCo ferrites substituted with Ce^{3+} and Dy^{3+} ions at $x = 0.02$, 0.06, and 0.08, some reduced peaks and consequently valleys appear with an increase in co-substitution ratios along with the frequency variation, while some fluctuations at low frequency occur, especially for $x = 0.02$. The dielectric loss has some deep and sharp valleys in the temperature transition region for $x = 0.04$ and some wavy peaks along with changes in both temperature and frequency for $x = 0.10$. At low frequency, the loss tangent is significantly larger, and at higher frequency, the effect becomes less due to reduced polarization in the higher applied field [43]. The noticed variations in tangential loss against frequency could be attributed to the mechanism of conduction in ferrites, similar to Koop's phenomenological model [44]. Identical trends, such as dielectric constant, were measured for dielectric loss tangent as well. Loss tangent reduces with increasing frequency due to strong correlations between dielectric behavior and conduction of ferrites. Compared to Koops model, the effect of grain boundaries at lower frequency is dominant and results in low conductivity at lower frequency and, therefore, shows a high loss tangent. Consequently, a large amount of energy is needed to exchange the electron among ferrous and ferric ions, which leads to a great energy losses. However, at higher frequencies, a small energy amount is needed for the exchange of electrons among ferrous and ferric ions, causing high conductivity and a small energy losses [45]. Such ferrite materials that have low dielectric loss are advantageous for high-frequency data read/write in electronics technology.

3.6. *Magnetic properties*

The loops of magnetization versus field (M–H) for the NiCo ferrite nanoparticles and $Ni_{0.5}Co_{0.5}Ce_xDy_xFe_{2-2x}O_4$ ($x \leq 0.10$) SFMSs are presented in Fig. 13. According to these curves, the values of saturation magnetization (M_s), remanent magnetization (M_r), and coercive field (H_c) of NiCo ferrite nanoparticles and $Ni_{0.5}Co_{0.5}Ce_xDy_xFe_{2-2x}O_4$ ($x \leq 0.10$) SFMSs are equal to about 51.4 and 23.5 emu/g, 18.5 and 8.1 emu/g, and 648.1 and 363.2 Oe, respectively. Obviously, M_s, M_r, and H_c are greater for NiCo ferrite nanoparticles compared to those for NiCo SFMSs. This is mostly because that the specific surface area of $Ni_{0.5}Co_{0.5}Fe_2O_4$ SFMSs is relatively small. Indeed, the current $Ni_{0.5}Co_{0.5}Fe_2O_4$ SFMSs prepared through the hydrothermal method and via template approach by using the carbon SFMSs as template showed smaller crystallite/particle size in

Table 3 – Mossbauer parameters for $Ni_{0.5}Co_{0.5}Ce_xDy_xFe_{2-2x}O_4$ ($x \leq 0.10$) SFMSs.

x	Sites	I.S. (±0.001) (mm/s)	Q.S. (±0.003) (mm/s)	B_{hf} (±0.04) (T)	Γ (±0.03) (mm/s)	R_A (%)
0.00	Sx- B_1: Fe^{+3}	0.317	0.004	48.457	0.416	9.819
	Sx- A: Fe^{+3}	0.292	−0.013	46.165	0.587	10.612
	Sx- B_2: Fe^{+3}	0.294	−0.033	43.081	0.589	23.509
	Sx- B_3: Fe^{+3}	0.341	−0.077	38.739	1.658	38.866
	Db: Fe^{+3}	0.321	0.838	–	1.2933	17.194
0.02	Sx- B_1: Fe^{+3}	0.315	0.021	47.115	0.714	8.775
	Sx- A: Fe^{+3}	0.293	0.04	44.404	0.599	12.058
	Sx- B_2: Fe^{+3}	0.35	−0.007	41.391	0.743	15.452
	Sx- B_3: Fe^{+3}	0.422	0.117	36.214	0.861	41.458
	Db: Fe^{+3}	0.331	0.635	–	0.834	22.257
0.04	Sx- B_1: Fe^{+3}	0.375	−0.051	50.968	0.327	9.4203
	Sx- A: Fe^{+3}	0.286	0.003	48.077	0.458	27.287
	Sx- B_2: Fe^{+3}	0.313	−0.032	43.237	0.926	42.407
	Sx- B_3: Fe^{+3}	0.279	0.033	26.01	0.925	16.421
	Db: Fe^{+3}	0.331	0.614	–	0.805	4.5647
0.06	Sx- B_1: Fe^{+3}	0.378	0.078	49.518	0.277	5.1697
	Sx- A: Fe^{+3}	0.281	0.022	46.519	0.402	28.935
	Sx- B_2: Fe^{+3}	0.318	−0.032	41.398	0.855	47.893
	Sx- B_3: Fe^{+3}	0.308	−0.045	26.006	0.935	15.54
	Db: Fe^{+3}	0.361	0.629	–	0.748	2.4623
0.08	Sx- B_1: Fe^{+3}	0.376	0.002	47.252	0.611	21.413
	Sx- A: Fe^{+3}	0.288	−0.01	41.514	0.856	29.304
	Sx- B_2: Fe^{+3}	0.342	−0.012	26.004	2.11	33.806
	Db: Fe^{+3}	0.32	0.766	–	0.874	15.477
0.1	Sx- B_1: Fe^{+3}	0.362	−0.07	45.933	0.611	20.105
	Sx- A: Fe^{+3}	0.279	−0.037	40.356	0.792	30.685
	Db: Fe^{+3}	0.33	0.613	–	0.537	49.21

(H_{hf}: hyperfine magnetic field. I.S: Isomer Shift. Q.S: Quadrupole Splitting. Γ: Line Width. R_A: Relative area).

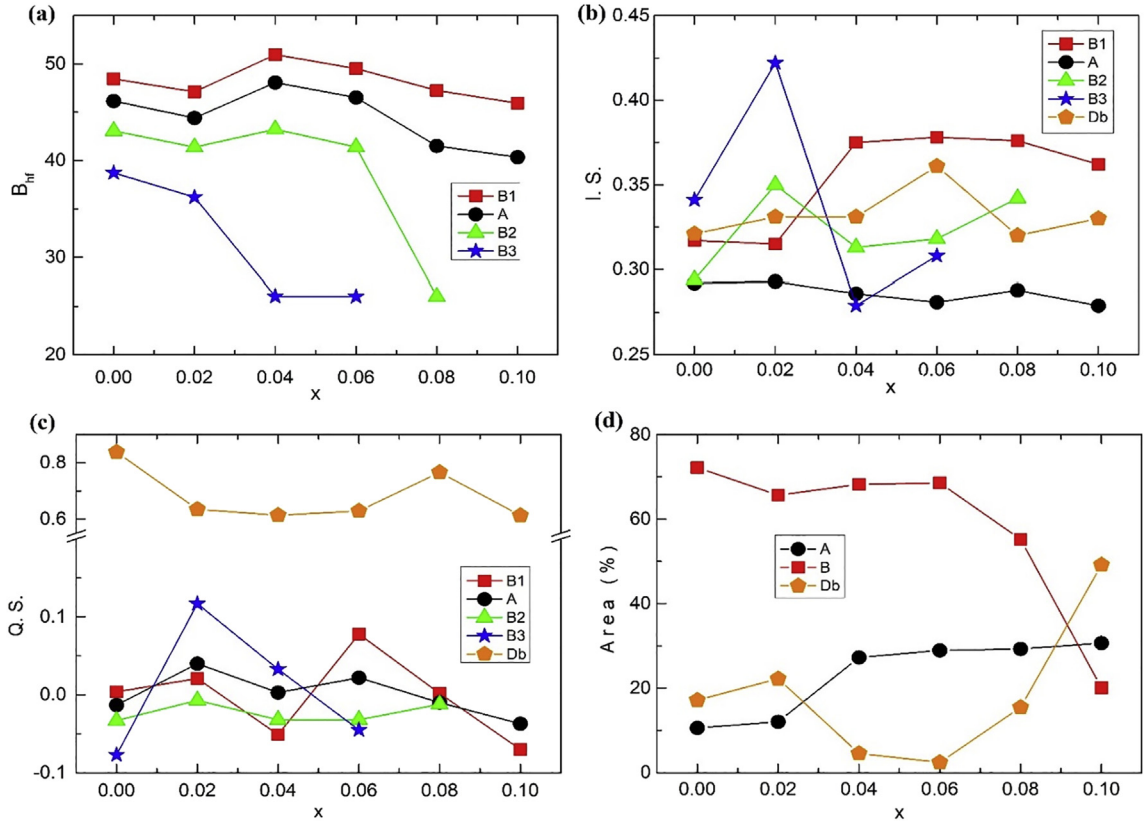

Fig. 7 – Variation of (a) Hyperfine Magnetic Field, (b) Isomer Shift, (c) Quadrupole Splitting, (d) Relative Area with Ce–Dy substitution in $Ni_{0.5}Co_{0.5}Ce_xDy_xFe_{2-2x}O_4$ ($x \leq 0.10$) SFMSs.

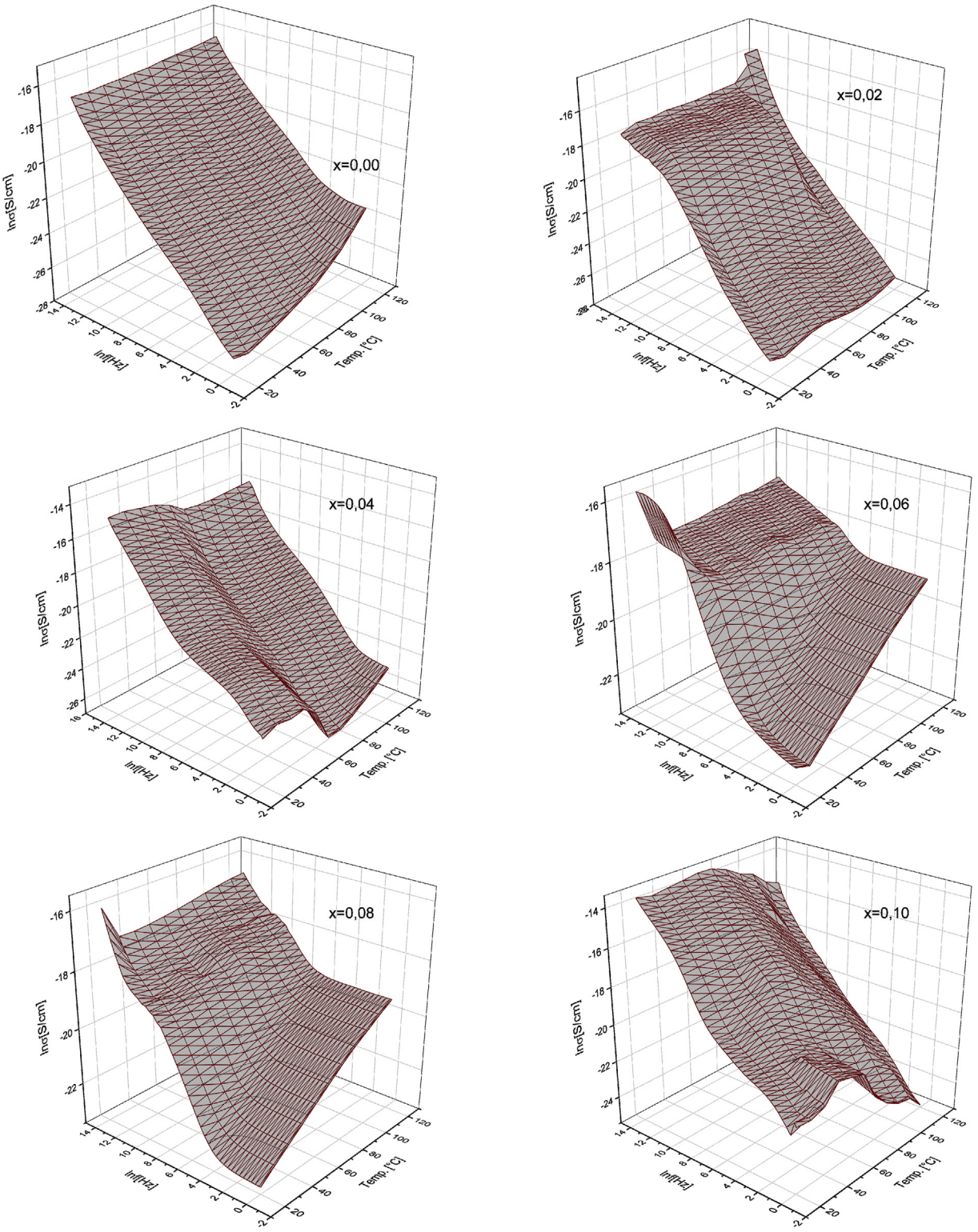

Fig. 8 – The ac conductivity of $Ni_{0.5}Co_{0.5}Ce_xDy_xFe_{2-2x}O_4$ ($x \leq 0.10$) SFMSs.

comparison to $Ni_{0.5}Co_{0.5}Fe_2O_4$ nanoparticles prepared via simply hydrothermal technique [46]. As the specific surface area becomes relatively small, and once the magnetic field is applied, it will be easier to change the direction of magnetic domains, leading to a smaller coercive field. In other words, the surface effects in nanostructured materials could conduce to the decline in M_s value. The existence of magnetically dead layers on the surfaces of nanoparticles and the effects of spins canting within the whole volume of the particle can produce decay in M_s value [47].

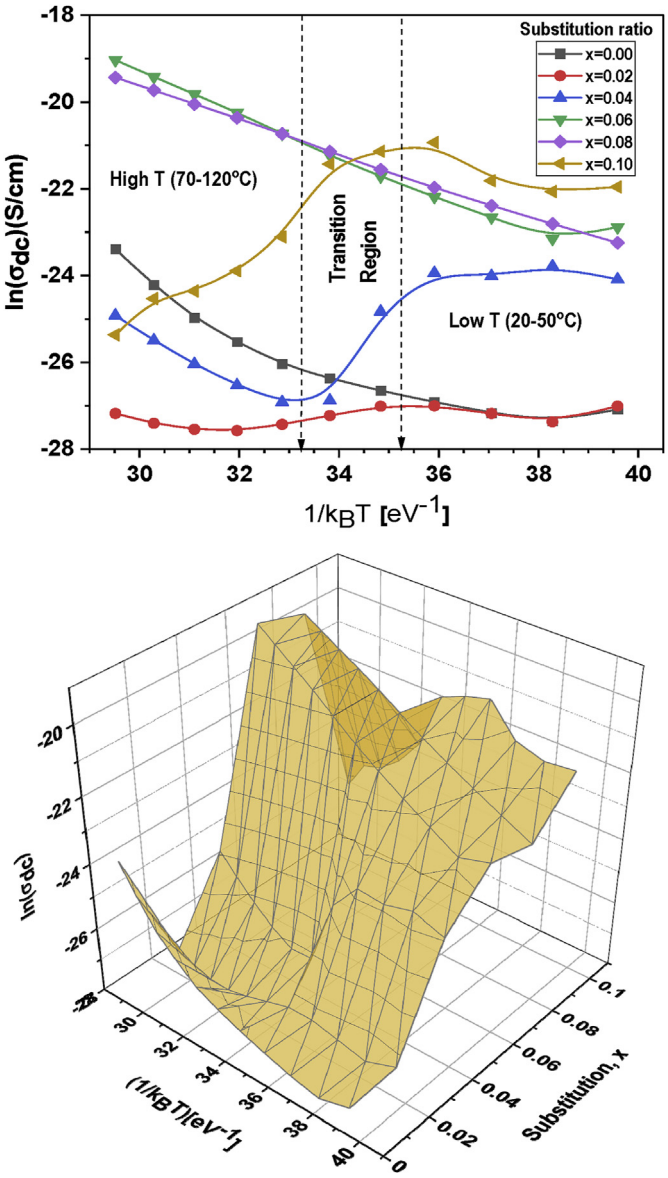

Fig. 9 – The dc conductivity of $Ni_{0.5}Co_{0.5}Ce_xDy_xFe_{2-2x}O_4$ (x ≤ 0.10) SFMSs.

M–H hysteresis loops for different prepared samples of $Ni_{0.5}Co_{0.5}Ce_xDy_xFe_{2-2x}O_4$ (x ≤ 0.1) SFMSs were investigated. Fig. 14 reveals the M–H curves that were registered under an applied magnetic field of ±10 kOe for all compositions of Ce^{3+}-Dy^{3+} ions substituted NiCo SFMSs. The magnetic behaviors of $Ni_{0.5}Co_{0.5}Ce_xDy_xFe_{2-2x}O_4$ (x ≤ 0.1) SFMSs are noticed to be narrow, confirming the soft magnetic nature of these products. Various prepared $Ni_{0.5}Co_{0.5}Ce_xDy_xFe_{2-2x}O_4$ (x ≤ 0.1) SFMSs displayed soft ferrimagnetic behavior. The S-shaped M–H loops for $Ni_{0.5}Co_{0.5}Ce_xDy_xFe_{2-2x}O_4$ (x ≤ 0.1) SFMSs products could be more saturated by applying magnetic field higher than 10 kOe. For the current case, we applied the law of approaching to saturation (LAS) to estimate the values of M_s [48,49]. This could be performed by plotting M vs. $1/H^2$ for diverse SFMSs and applying the following expression at the regions of high magnetic fields, as shown in Fig. 15 [50,51]:

$$M = M_s\left(1 - \frac{\alpha}{H^2}\right) \quad (4)$$

Here, the factor 'α' is governed by the magnetocrystalline anisotropy (K_{eff}). The slope and the intercept in M vs. $1/H^2$ plots will lead to extract the values of α and M_s, respectively. Once the 'α' factor is extracted, the value of K_{eff} could be calculated using the following expression [52,53]:

$$K_{eff} = M_s\left(\frac{15\alpha}{4}\right)^{0.5} \quad (5)$$

The magnetic parameters namely M_s, M_r, magnetic moment per unit formula in Bohr magneton (n_B), and effective anisotropy constant (K_{eff}) are extracted and calculated by using M–H data and their variations with respect to Ce–Dy content are illustrated in Fig. 16. It is noticed from this figure that M_s value increases with the increment in Ce–Dy

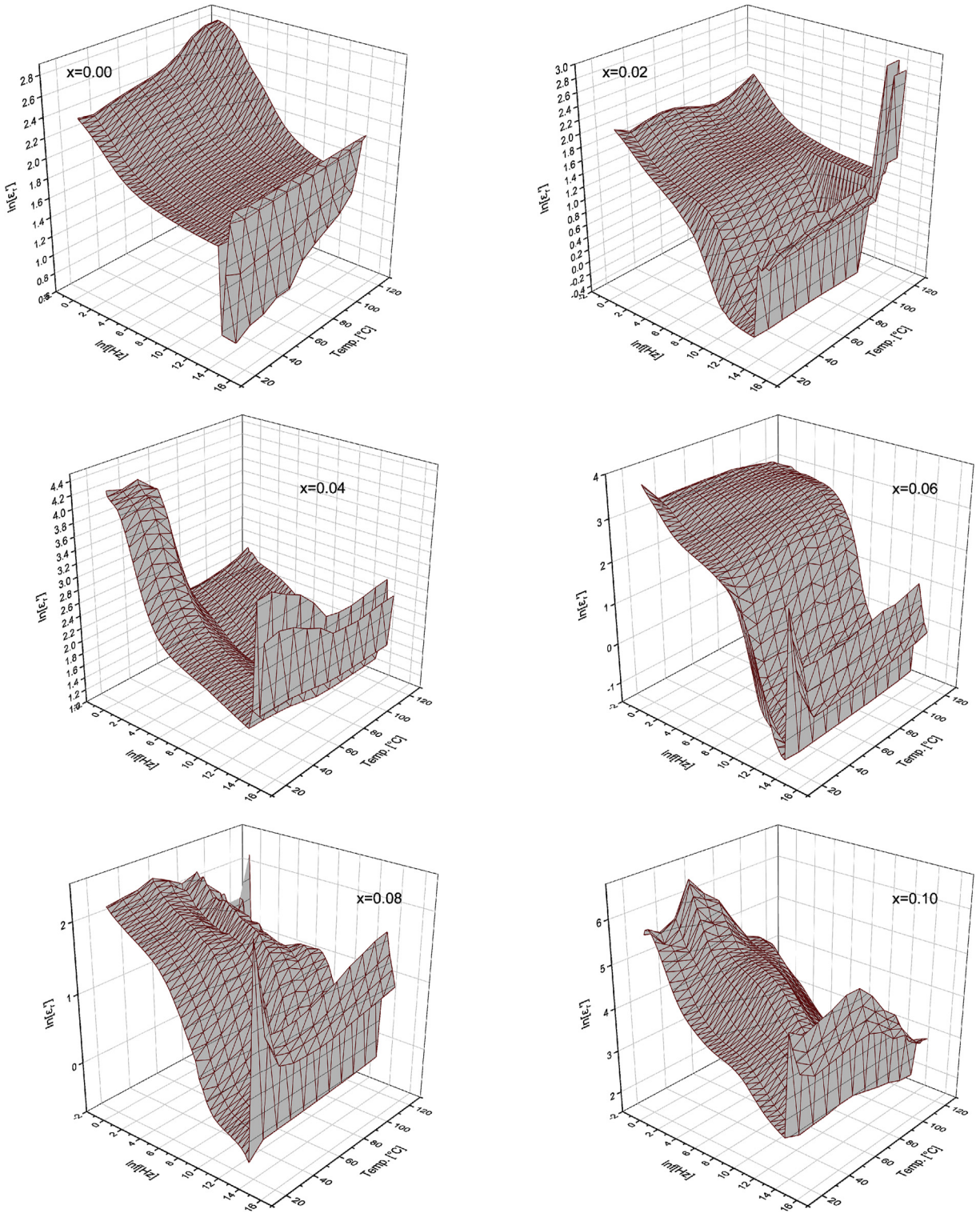

Fig. 10 – Dielectric constant of $Ni_{0.5}Co_{0.5}Ce_xDy_xFe_{2-2x}O_4$ ($x \leq 0.10$) SFMSs.

content with the NiCo SFMSs, reaching its maximum at x = 0.04 with a value of about 31.2 emu/g. With the further increment in the concentration of Ce–Dy within the NiCo SFMSs (i.e., x > 0.04), M_s value decreases. Also, the M_r value showed an analogous tendency to that of M_s. Generally, intrinsic and extrinsic factors like the distribution of metal ions among the sublattice sites, super-exchange interactions, morphology, porosity, crystallites/particles size, defects, composition, and homogeneity of the produced ferrites are responsible for the variations in magnetic parameters with respect to the substituting content [54–56]. Usually, for nanostructured materials, the surface effects play an

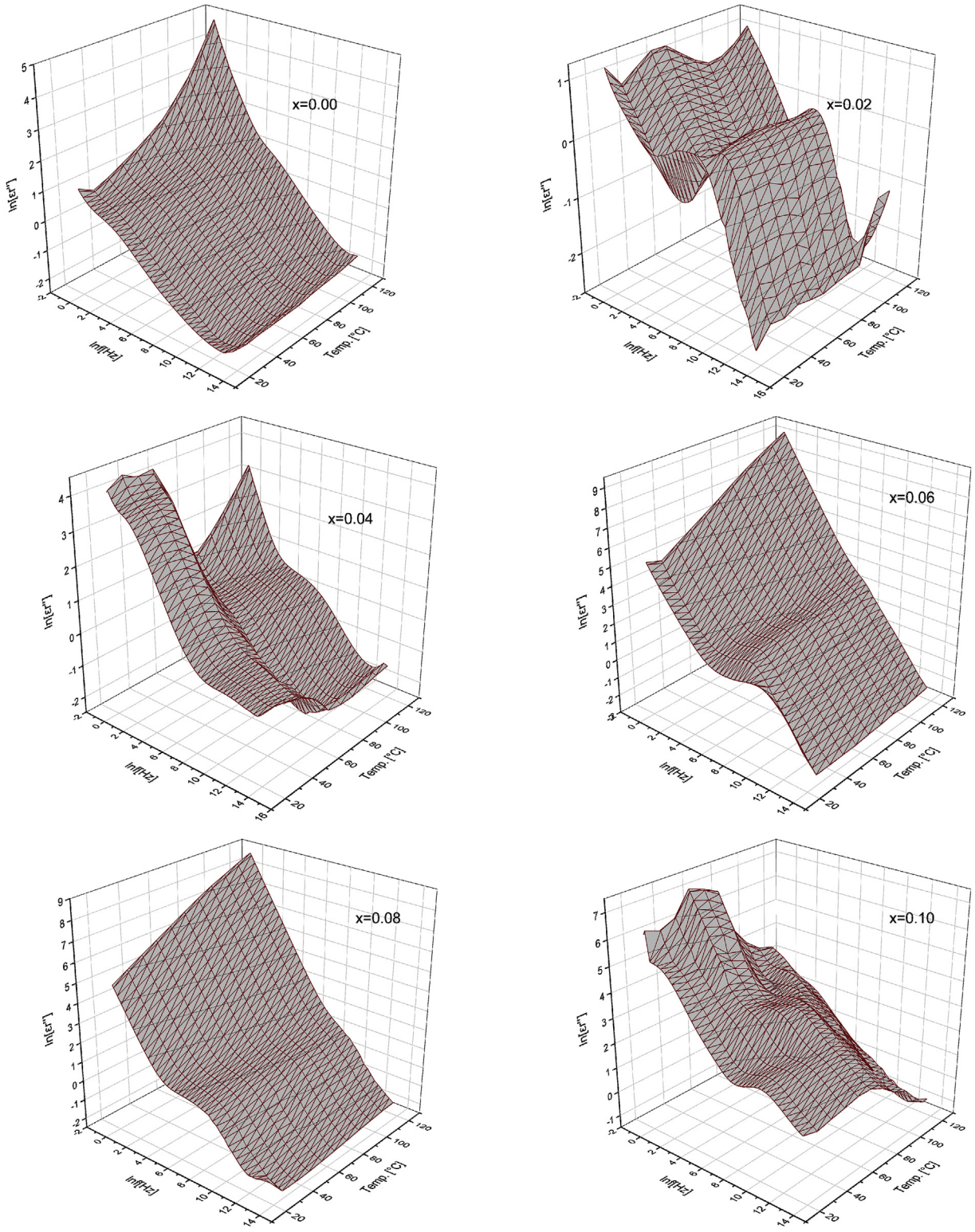

Fig. 11 – Dielectric loss of $Ni_{0.5}Co_{0.5}Ce_xDy_xFe_{2-2x}O_4$ ($x \leq 0.10$) SFMSs.

important impact on the value of M_s. As the crystallite size decrease, the M_s value will decrease and vice versa. It could be noticed from the XRD analysis that the crystallites size decreased up to $x = 0.04$ and then increased with the further rise in Ce–Dy content. The decrease in crystallites/particles size suggests an increase in the surface-to-volume ratio among atoms. Because of this, the surface effects will be prominent [54]. The reverse case will happen when the crystallites/particles size increases. The spins canting effect in the whole crystallite volume and the presence of magnetic

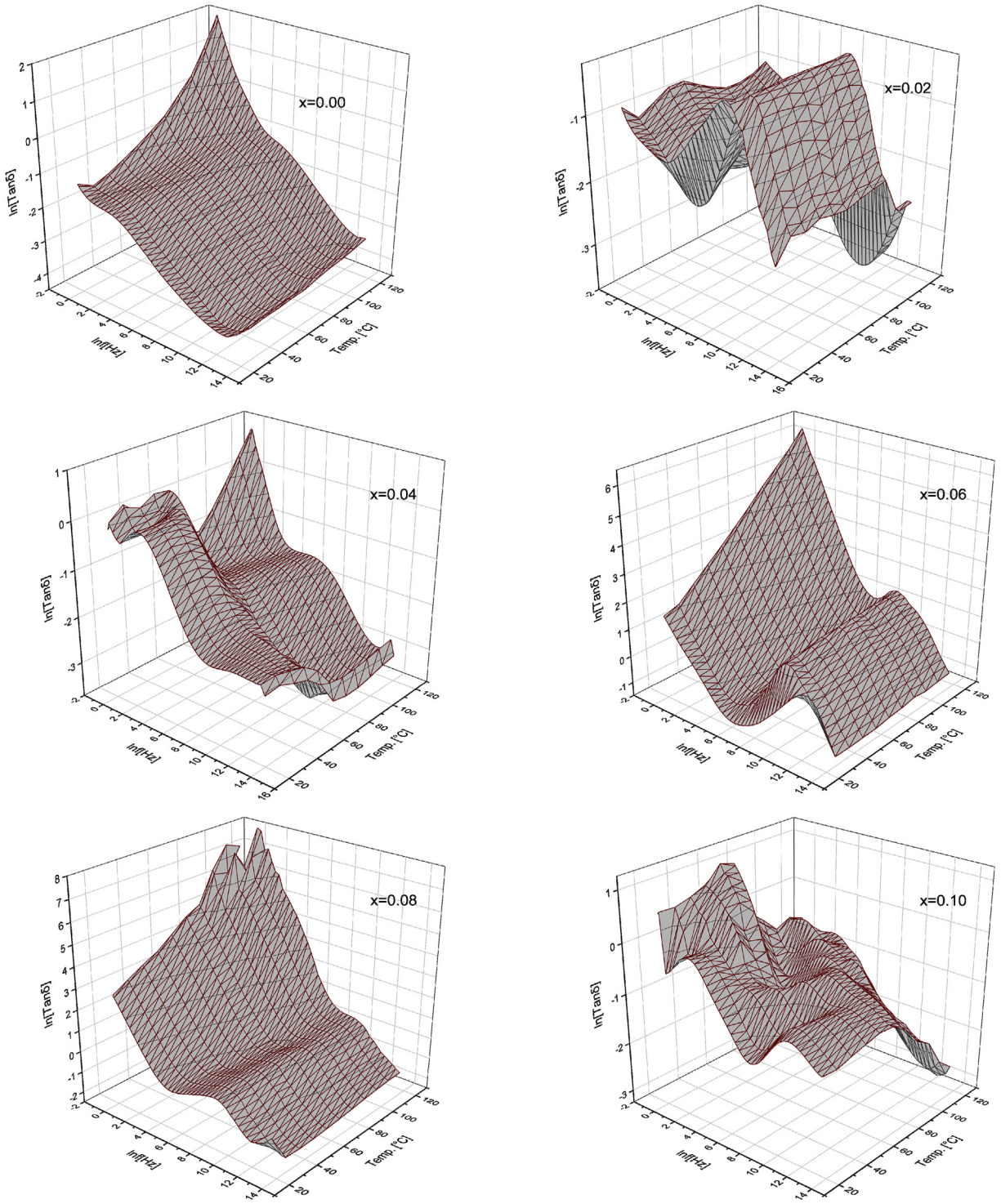

Fig. 12 – Dielectric tangent loss of $Ni_{0.5}Co_{0.5}Ce_xDy_xFe_{2-2x}O_4$ ($x \leq 0.10$) SFMSs.

dead layer on the surface of nanomaterial can provoke a reduction in the M_s value [36].

The increase and then the reduction in M_s values could be also associated to the incorporation of RE^{3+} ions. Usually, in spinel ferrites, when the ions of Fe^{3+} are substituted by ions of RE^{3+} displaying greater magnetic moments, the magnetization of RE^{3+} ions substituted NiCo ferrites would enhance. Whereas, when the magnetic moments of RE^{3+} ions are smaller than those of Fe^{3+} ions, the situation will be reversed, in which the magnetization of RE^{3+} ions substituted NiCo ferrites would reduce. Occasionally, this trend is not presented by all RE ions substituting spinel ferrites. Generally, the RE^{3+} ions, once are incorporated within the spinel ferrite lattice, tend to reside in the octahedral B site [11,57,58]. The ions of Fe^{3+}, Ce^{3+}, and Dy^{3+} display magnetic moments of about 5, 2.5, and 10.5 μ_B, respectively. Ce^{3+} ions display magnetic

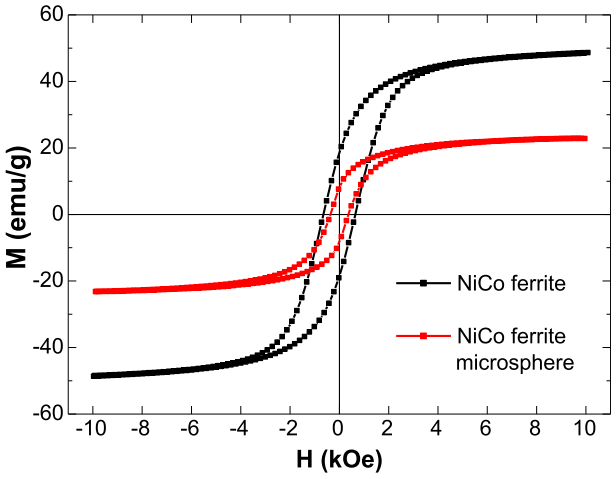

Fig. 13 – M-H graph of both NiCo ferrite and NiCo ferrite microsphere.

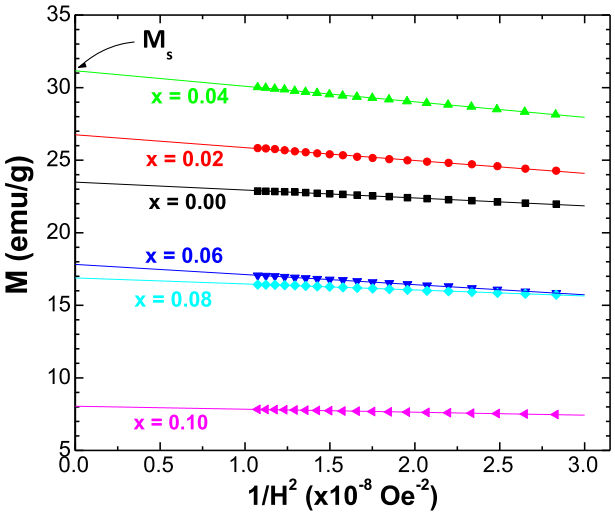

Fig. 15 – M vs. $1/H^2$ plots for different $Ni_{0.5}Co_{0.5}Ce_xDy_xFe_{2-2x}O_4$ ($x \leq 0.10$) SFMSs. The solid lines represent the S-W fit in which the intercept leads to extract the value of $Ni_{0.5}Co_{0.5}Ce_xDy_xFe_{2-2x}O_4$ ($x \leq 0.10$) SFMSs.

moment smaller than that of Fe^{3+} ions, while Dy^{3+} ions have greater magnetic moment as compared to Fe^{3+} ions. In NiCo spinel ferrites, the distribution among A and B sites is anti-parallel while those among A-A as well as B-B is parallel. This conduces to the ordered arrangement of ferrimagnetism. As mentioned above, the ions with greater ionic radii are largely residing in B sites. Therefore, the RE^{3+} ions such as Ce^{3+} and Dy^{3+} ions tend to reside in the B sites by substituting Fe^{3+} ions. The principal contributions to the magnetic characteristics come from the ions of Fe^{3+} that are existing at the B sites of spinel ferrite lattice. The average magnetic moments of Ce^{3+} and Dy^{3+} ions are higher than that of Fe^{3+} ions, hence the super-exchange interactions could increase significantly upon the incorporation of Ce^{3+} and Dy^{3+} ions. This could explain the initial increase of magnetization with lower Ce–Dy doping content. Nevertheless, it is noticed that the M_s and M_r values decrease at higher Ce–Dy doping contents ($x \geq 0.06$). The magnetic features of the current products at higher content ($x \geq 0.06$) could be described based on Neel's model [59,60]. In accordance with this model, the calculated magneton number is provided by $n_B = M_B - M_A$, in which M_B and M_A are the magnetic moments of B and A sublattices,

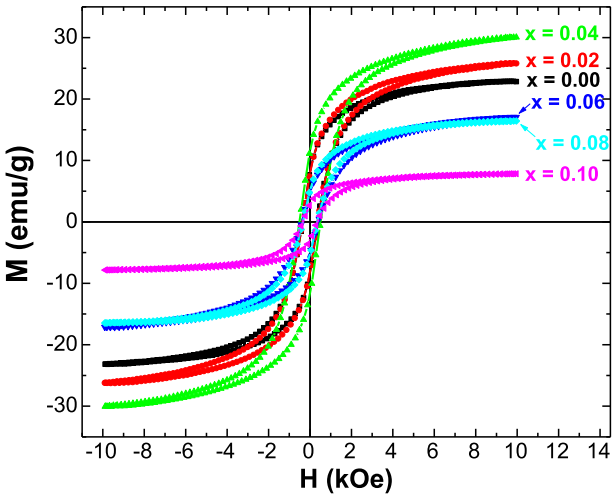

Fig. 14 – M–H curves for different $Ni_{0.5}Co_{0.5}Ce_xDy_xFe_{2-2x}O_4$ ($0.00 \leq x \leq 0.10$) SFMSs.

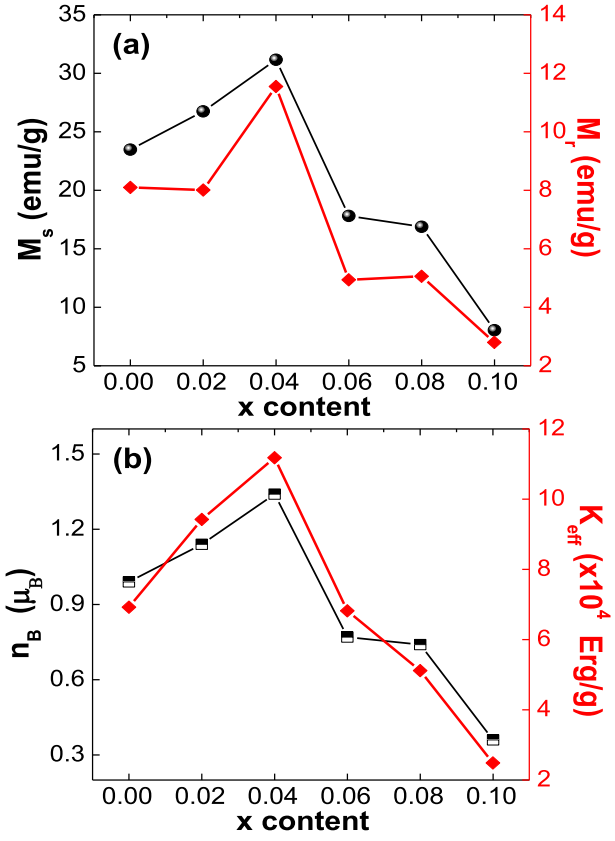

Fig. 16 – Variations of (a) M_s and M_r and (b) n_B and K_{eff} for different $Ni_{0.5}Co_{0.5}Ce_xDy_xFe_{2-2x}O_4$ ($x \leq 0.10$) SFMSs.

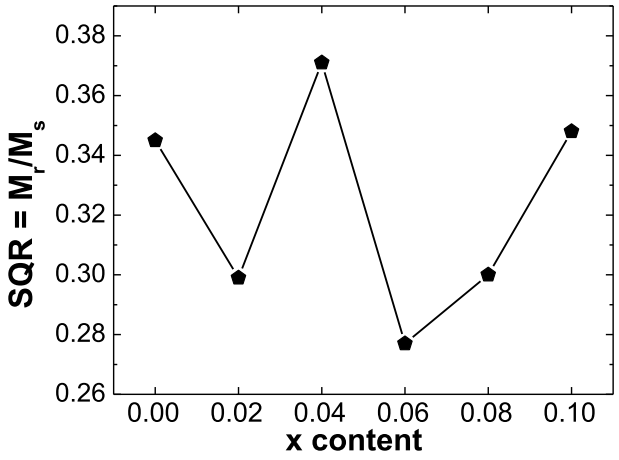

Fig. 17 – Calculated SQR values for different $Ni_{0.5}Co_{0.5}Ce_xDy_xFe_{2-2x}O_4$ ($x \leq 0.10$) SFMSs.

respectively. In spinel crystal structure, three exchange interactions between A and B sublattices are existing, namely A-A, B-B, and A-B, wherein the strength of A-B super-exchange interactions are much greater than that of A-A and B-B interactions. At higher Ce–Dy doping contents ($x \geq 0.06$), the rise of the concentration of Ce^{3+} and Dy^{3+} ions could cause a migration of some Ni^{2+} ions from B sites to A sites. Consistent with the previous reports, Ni spinel ferrites are partially inverse spinel where high fraction of Ni^{2+} ions resides in B sites and a small Ni^{2+} ions fraction resides in A sites while each half fraction of Fe^{3+} ions occupy the A and B sites, as follow as $(Ni_{0.05}Fe_{0.95})^A[Ni_{0.95}Fe_{1.05}]^BO_4$ [61]. On the other hand, the Co spinel ferrites are perfect inverse spinel as follow $(Fe_1)^A$ $[Co_1Fe_1]^BO_4$ [61]. Additionally, the tiny size of particles endorses the mixed spinel structure of Ni ferrites. Consequently, the ions of Ni^{2+} tend to reside also within the A sites and could be easily pushed from B sites to A sites. This could result in enhancing the magnetic moments of A sublattices (M_A), hence $n_B = M_B - M_A$ will reduce, and therefore, the M_s and M_r values will decrease at higher Ce–Dy contents ($x \geq 0.06$).

The values of n_B, presented in Fig. 15b, were calculated through the following relation [62,63]:

$$n_B = \frac{Mw \times M_s}{5585} \quad (6)$$

wherein Mw is the molecular weight of a specific composition. It is noticed from Fig. 15a that the experimental magneton number follows the tendency of M_s value. The magnetic moment is increased by the Ce–Dy doping within the NiCo SFMSs. It increased from $x = 0.00$ up to $x = 0.04$. This could be ascribed to the strengthening of magnetic interactions among the A and B sites due to that Dy^{3+} ions have higher magnetic moment in comparison to Fe^{3+} ions. For Ce–Dy content of $x \geq 0.06$, the n_B value was found to decrease, indicating a weakening of magnetic interactions among A and B sites at higher doping contents. This weakening is most probably attributed to higher amount of Ce^{3+} ions that display lower magnetic moment in comparison to Fe^{3+} ions. Furthermore, since the rare-earth ions of Ce^{3+} and Dy^{3+} possess greater ionic radii in comparison to Fe^{3+} ions, the substitution of Fe^{3+} ions by higher concentration of RE ions could provoke a weakening in A-B magnetic interactions. The incorporation of lower contents of Ce and Dy elements could be considered as being magnetic ions substitution within the spinel structure that enhance the exchange interactions of magnetic ions among the A and B sites, provoking an improvement of M_s and M_r magnitudes. Whereas, at high Ce–Dy concentrations, the inclusion of Ce^{3+} and Dy^{3+} ions could be considered as being non-magnetic ions doped into the spinel structure that weaken the A-B exchange interactions and hence conduce to a decline in M_s and M_r values.

It would be noted that the spin-orbit coupling is produced by the inclusion of RE ions, Ce and Dy, by transforming the collinear ferrimagnetic arrangement into non-collinear ferrimagnetic order of spins on the B sites [47]. Typically, as discussed above, for NiCo spinel ferrites, the majority of Ni^{2+} ions reside in the B sites and a minor content of them occupies the A sites, all Co^{2+} ions reside in B sites, thus, the residence of higher amount of Ce^{3+} and Dy^{3+} ions within the B sites will distort the collinear arrangement of spins and diminishes the

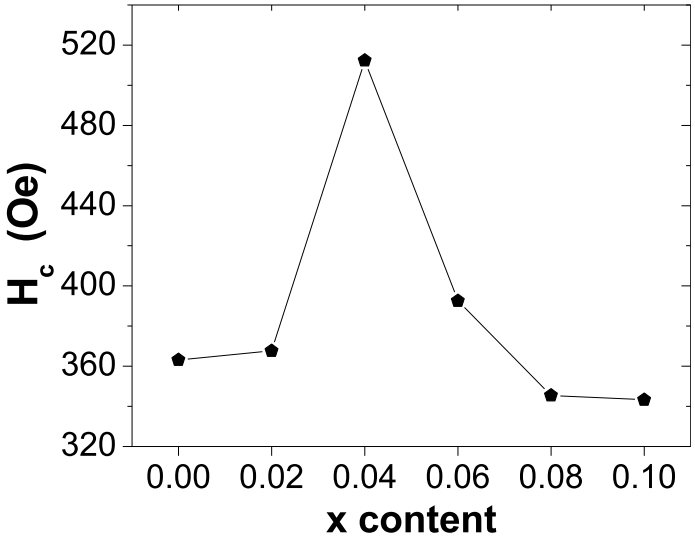

Fig. 18 – Evolutions in H_c values against the content of Ce^{3+}-Dy^{3+} for different $Ni_{0.5}Co_{0.5}Ce_xDy_xFe_{2-2x}O_4$ ($x \leq 0.10$) SFMSs.

M_s value. Furthermore, no further transportation of Fe^{3+} ions towards the B sites is happening, leading there to a decrease in M_s value.

It is found that the non-substituted $Ni_{0.5}Co_{0.5}Fe_2O_4$ SFMSs exhibit K_{eff} value of approximately 6.92×10^4 Erg/g. The K_{eff} value enhances upon the incorporation of Ce^{3+} and Dy^{3+} ions, reaching its maximum value of 11.18×10^4 Erg/g for $x = 0.04$. Afterward, K_{eff} diminishes with the further increase in Ce^{3+} and Dy^{3+} ion concentration. It is obvious also that K_{eff} values display similar variation tendency of M_s value. This could explain the observed trend in M_s with respect to Ce^{3+} and Dy^{3+} substituting ions content.

Fig. 17 depicts the values of squareness ratio (SQR) for different compositions, which are calculated by performing the ratio between M_r and M_s values for each composition. In accordance with previous theoretical calculations [64,65], it was stated that SQR value than 0.5 implies that the system comprises of particles with single-magnetic domain (SMD) structure, while SQR greater than 0.5 implies a system consisting of particles with multi-magnetic domain (MMD) structure. The SQR values, that are smaller than 0.5, indicated the manifestation of single-magnetic domain (MMD) particles within the studied SFMSs [66,67].

Fig. 18 presents the evolutions in H_c values with respect to the content of Ce^{3+} and Dy^{3+} ions. It has been reported that H_c value is affected by numerous issues like magnetic domains, anisotropy, micro-strains, particles/grains size, distribution of size, magneto-crystallinity, etc. [68–70]. The incorporation of RE ions will provoke lattice distortions within the spinel ferrite [71,72]. The diminution in the crystal unit symmetry upon the inclusion of Ce^{3+} and Dy^{3+} within NiCo SFMSs could conduce to magneto-crystalline anisotropy that leads to greater coercive field in comparison to pristine NiCo SFMSs. It is shown that H_c value of the produced SFMSs rises with substitution of Ce–Dy ions within the NiCo ferrite. The coercive field of product attains its greatest level for $x = 0.04$ content. It improves from about 363.2 Oe at $x = 0.00$ to 512.4 Oe at $x = 0.04$. After that, the H_c value is noticed to reduce for higher concentration of Ce–Dy within the NiCo SFMSs (i.e., $x > 0.04$). This tendency could be related to the variation in magneto-crystalline anisotropy (K_{eff}) with respect to Ce–Dy doping. As shown in Figs. 15b and 17, K_{eff} and H_c display similar tendency with respect to Ce^{3+} and Dy^{3+} ions doping.

4. Conclusion

The hydrothermal method has been applied to synthesize a series of $Ni_{0.5}Co_{0.5}Ce_xDy_xFe_{2-2x}O_4$ ($x \leq 0.10$) SFMSs. XRD analysis illustrated the structure of carbon and $Ni_{0.5}Co_{0.5-}Ce_xDy_xFe_{2-2x}O_4$ ($x \leq 0.10$) SFMSs. Further analysis of NPs SFMSs disclosed the spherical shape, with a narrow size distribution an average particle size of 10 nm. The diffuse reflectance measurements showed a strong light absorption after 650 nm. Also, it is found that the magnitude of energy band gap E_g increased considerably with increasing concentration of Ce–Dy ions. The hyperfine interactions of $Ni_{0.5-}Co_{0.5}Ce_xDy_xFe_{2-2x}O_4$ ($x \leq 0.10$) SFMSs were investigated with Mossbauer spectroscopy, revealing the preferential occupancy of Dy^{3+} and Ce^{3+} ions at the octahedral B site. The hyperfine interactions of A and B sites show decrease with rising concentration of doping ions. The local symmetry of the host material is not influenced by the rare-earth substitutions. The analysis of M-H loops disclosed ferrimagnetic behavior for different SFMSs. It is noticed that all M_s, M_r, and H_c get increased from $x = 0.00$ up to 0.04 Ce^{3+} -Dy^{3+} content, and then decreased with further increase of Ce–Dy contents. The determined experimental magneton numbers and effective magneto-crystalline anisotropy agree with the variations in different magnetic parameters. The surface spins effect, the evolutions in crystallite/particle size, the distribution of magnetic ions into the different sublattices, the evolutions of magneto-crystalline anisotropy, and the variations in magnetic moment (n_B) showed great influence on the variations in magnetic parameters (M_s, M_r, and H_c). Squareness ratio (SQR) values were established to be smaller than the predicted theoretical value of 0.5 for all samples, indicating single-magnetic domain (SMD) characteristic of NiCo SFMSs. The co-substitution of rare-earth ions Ce and Dy in NiCo SFMSs has had a significant effect on the electrical and dielectric properties. The ac conductivity obeys the power law rule of frequency, depending strongly on co-substitution ratios. The dc conductivity decreases with the variation of $(k_BT)^{-1}$ except the co-substitution ratio of $x = 0.10$. It is clear that DC conductivity is highly dependent on both temperature and co-substitution ratios. It has been observed that dielectric parameters such as dielectric constant and loss tangent reduce with the rise in frequency occurring in the normal behavior of ferrites. The dielectric constant of NiCo SFMSs indicates the well-known dielectric dispersion of ferrites by frequency.

Declaration of Competing Interest

There are no conflicts of interest to declare.

Acknowledgment

The authors acknowledge the financial supports provided by the Deanship for Scientific Research of Imam Abdulrahman Bin Faisal University (Project application No. 2020-164-IRMC).

REFERENCES

[1] Mkwae PS, Kortidis I, Kroon RE, Leshabane N, Jozela M, Swart HC, et al. Insightful acetone gas sensing behaviour of Ce substituted $MgFe_2O_4$ spinel nano-ferrites. J Mater Res Technol 2020;9(6):16252–69.

[2] Gao J, Du Z, Ma S, Cheng F, Li P. High-efficiency leaching of valuable metals from saprolite laterite ore using pickling waste liquor for synthesis of spinel-type ferrites MFe_2O_4 with excellent magnetic properties. J Mater Res Technol 2021;10:988–1001.

[3] Kefeni KK, Mamba BB. Photocatalytic application of spinel ferrite nanoparticles and nanocomposites in wastewater treatment: Review. Sustain Mater Technol 2020;23:e00140.

[4] Valente F, Astol L, Simoni E, Danti S, Franceschini V, Chicca M, et al. Nanoparticle drug delivery systems for inner

ear therapy: an overview. J Drug Deliv Sci Technol 2017;39:28–35.
[5] Demirelli M, Karaoğlu E, Baykal A, Sozeri H, Uysal E. Synthesis, characterization, and catalytic activity of $CoFe_2O_4$-APTES-Pd magnetic recyclable catalyst. J Alloys Compd 2014;582:201–7.
[6] Sutka A, Gross A. Spinel ferrite oxide semiconductor gas sensors. Sensor Actuator B Chem 2016;222:95–105.
[7] Routray KL, Saha S, Behera D. Green synthesis approach for nano sized $CoFe_2O_4$ through aloe vera mediated sol-gel auto combustion method for high frequency devices. Mater Chem Phys 2019;224:29–35.
[8] Domínguez-Arvizu JL, Jiménez-Miramontes JA, Salinas-Gutiérrez JM, Meléndez-Zaragoza MJ, López-Ortiz A, Collins-Martínez V. Study of $NiFe_2O_4$ nanoparticles optical properties by a six-flux radiation model towards the photocatalytic hydrogen production. Int J Hydrogen Energy 2019;44:12455–62.
[9] Ng QH, Lim JK, Ahmad AL, Ooi BS, Low SC. Magnetic nanoparticles augmented composite membranes in removal of organic foulant through magnetic actuation. J Membr Sci 2015;493:134–46.
[10] Somvanshi SB, Patade SR, Andhare DD, Jadhav SA, Khedkar MV, Kharat PB, et al. Hyperthermic evaluation of oleic acid coated nano-spinel magnesium ferrite: enhancement via hydrophobic-to-hydrophilic surface transformation. J Alloys Compd 2020;835:155422.
[11] Almessierea MA, Slimani Y, Guner S, Sertkol M, Demir Korkmaz A, Shirsath Sagar E, et al. Sonochemical synthesis and physical properties of $Co_{0.3}Ni_{0.5}Mn_{0.2}Eu_xFe_{2-x}O_4$ nano-spinel ferrites. Ultrason Sonochem 2019;58:104654.
[12] Almessiere MA, Demir Korkmaz A, Slimani Y, Nawaz M, Ali S, Baykal A. Magneto-optical properties of Rare Earth metals substituted Co-Zn spinel nanoferrites. Ceram Int 2019;45(3):3449–58.
[13] Almessiere MA, Slimani Y, Korkmaz AD, Guner S, Sertkol M, Shirsath Sagar E, et al. Structural, optical, and magnetic properties of Tm^{3+} substituted cobalt spinel ferrites synthesized via sonochemical approach. Ultrason Sonochem 2019;54:1–10.
[14] Khan MK. Structural and microwave absorption properties of $Ni_{(1-x)}Co_{(x)}Fe_2O_4$ ($0.0 \leq x \leq 0.5$) nanoferrites synthesized via co-precipitation route. J Alloys Compd 2011;509:3393–7.
[15] Nawale AB, Kanhe NS, Raut SA, Bhoraskar SV, Das AK, Mathe VL. Investigation of structural, optical, and magnetic properties of thermal plasma synthesized Ni-Co spinel ferrite nanoparticles. Ceram Int 2017;43:6637–47.
[16] Matli PR, Zhou X, Shiyu D, Huang Q. Fabrication, characterization, and magnetic behaviour of porous $ZnFe_2O_4$ hollow ferrite microspheres. Int Nano Lett 2015;5:53–9.
[18] Lou XW, Archer LA, Yang Z. Hollow micro-/nanostructures: synthesis and applications. Adv Mater 2008;20:3987–4019.
[19] Zhang Z, Wang Y, Tan Q, Zhong Z, Su F. Facile solvothermal synthesis of mesoporous manganese ferrite ($MnFe_2O_4$) ferrite microspheres as anode materials for lithium-ion batteries. J Colloid Interface Sci 2013;398:185–92.
[20] Mu GH, Pan XF, Shen HG, Gu MY. Preparation, and magnetic properties of composite powders of hollow ferrite microspheres coated with barium ferrite. Mater Sci Eng A 2007;445–446:563–6.
[21] Duan H, Zhou F, Cheng X, Chen G, Li Q. Preparation of hollow microspheres of Ce^{3+} doped NiCo ferrite with high microwave absorbing performance. J Magn Magn Mater 2017;424:467–71.
[22] Wang SR, Wang LW, Yang TL, Liu XH, Zhang J, Zhu BL, et al. Porous α-Fe_2O_3 hollow ferrite microspheres and their application for acetone sensor. J Solid State Chem 2010;183:2869–76.
[23] Kang YF, Wang LW, Wang YS, Zhang HX, Wang Y, Hong DT, et al. Construction, and enhanced gas sensing performances of CuO-modified α-Fe_2O_3 hybrid hollow spheres. Sens Actuators B 2013;177:570–6.
[24] Wang F, Liu J, Kong J, Zhang Z, Wang X, Itoh M, et al. Template free synthesis and electromagnetic wave absorption properties of monodispersed hollow magnetite nano-spheres. J Mater Chem 2011;21:4314.
[25] Zhang Y, Huang Z, Tang F, Ren J. Ferrite hollow spheres with tunable magnetic properties. Thin Solid Films 2006;515:2555–61.
[26] Titirici MM, Antonietti M, Thomas A. A generalized synthesis of metal oxide hollow spheres using a hydrothermal approach. Chem Mater 2006;18:3808–12.
[27] Slimani Y, Almessiere MA, Sertkol M, Shirsath Sagar E, Baykal A, Nawaz M, et al. Structural, magnetic, optical properties and cation distribution of nanosized $Ni_{0.3}Cu_{0.3}Zn_{0.4}Tm_xFe_{2-x}O_4$ ($0.0 \leq x \leq 0.10$) spinel ferrites synthesized by ultrasound irradiation. Ultrason Sonochem 2019;57:203–11.
[28] Kubelka P. New contributions to the optics intensely light scattering materials Part I. J Opt Soc Am 1948;38:448–57.
[29] Kubelka P, Munk F. Ein beitrag zur optik der farbanstriche. Tech Phys 1931;12:593.
[30] Tauc J, Grigorovici R, Vancu A. Optical properties and electronic structure of amorphous germanium. Phys Status Solidi 1966;15:627–37.
[31] Auwal IA, Baykal A, Güner S, Sertkol M, Sözeri H. Magneto-optical properties of $BaBi_xLa_xFe_{12-2x}O_{19}$ ($0.0 \leq x \leq 0.5$) hexaferrites. J Magn Magn Mater 2016;409:92–8.
[32] Auwal IA, Güngüneş H, Güner S, Shirsath Sagar E, Sertkol M, Baykal A. Structural, magneto-optical properties and cation distribution of $SrBi_xLa_xY_xFe_{12-3x}O_{19}$ ($0.0 \leq x \leq 0.33$) hexaferrites. Mater Res Bull 2016;80:263–72.
[33] Li X, Hou Y, Zhao Q, Wang L. A general, one-step and template-free synthesis of sphere-like zinc ferrite nanostructures with enhanced photocatalytic activity for dye degradation. J Colloid Interface Sci 2011;358:102.
[34] Ushakov MV, Senthilkumar B, Kalai Selvan R, Felner I, Oshtrakh MI. Mossbauer spectroscopy of $NiFe_2O_4$ nanoparticles: the effect of Ni^{2+} in the Fe^{3+} local microenvironment in both tetrahedral and octahedral sites. Mater Chem Phys 2017;202:159.
[35] Kumar H, Srivastava RC, Singh jP, Negi P, Agrawal HM, Das D, et al. Structural and magnetic study of dysprosium substituted cobalt ferrite nanoparticles. J Magn Magn Mater 2016;401:16–21.
[36] Amiri S, Shokrollahi H. Magnetic and structural properties of RE doped Co-ferrite (RE=Nd, Eu, and Gd) nanoparticles synthesized by co-precipitation. J Magn Magn Mater 2013;345:18–23.
[37] Hashim M, Ahmed A, Ali SA, Shirsath SE, Ismail MM, Kumar R, et al. Structural, optical, elastic, and magnetic properties of Ce and Dy doped cobalt ferrites. J Alloys Compd 2020;834:155089.
[38] Patil ND, Velhal NB, Tarwar NL, Puri Vijaya R. Dielectric and magnetic properties of Co substituted Ni-Cd-ferrite prepared by solution combustion method. Int J Eng Inn Tech 2014;3:73–7.
[39] Deonikar VG, Kulkarni VD, Rathod SM, Kim H. Fabrication and characterizations of structurally engineered lanthanum substituted nickel-cobalt ferrites for the analysis of electric and dielectric properties. Inorg Chem Commun 2020;119:108074.
[40] Naik CC, Salker AV. Investigation of the effect of fractional In^{3+} ion substitution on the structural, magnetic, and dielectric properties of Co-Cu ferrite. J Phys Chem Solid 2019;133:151–62.

[41] Koops CG. On the dispersion of resistivity and dielectric constant of some semiconductors at audiofrequencies. Phys Rev 1951;83:121–4.
[42] Ul S, Kumar K, Murugesan G, Kalainathan S. A study on dielectric and magnetic properties of lanthanum substituted cobalt ferrite. J Alloys Compd 2017;701:612–8.
[43] Singh N, Agarwal A, Sanghi S, Khasa S. Dielectric loss, conductivity relaxation process and magnetic properties of Mg substituted Ni–Cu ferrites. J Magn Magn Mater 2012;324:2506.
[44] Kahn ML, Zhang Z. Synthesis, and magnetic properties of $CoFe_2O_4$ spinel ferrite nanoparticles doped with lanthanide ions. J Appl Phys Lett 2001;78:3651–3.
[45] Kambale RC, Shaikh PA, Bhosale CH, Rajpure KY, Kolekar YD. The effect of Mn substitution on the magnetic and dielectric properties of cobalt ferrite synthesized by an auto combustion route. Smart Mater Struct 2009;18:115028.
[46] Almessiere MAM, Slimani Y, Sertkol M, Nawaz M, Sadaqat A, Baykal A, et al. Effect of Nb^{3+} substitution on the structural, magnetic, and optical properties of $Co_{0.5}Ni_{0.5}Fe_2O_4$ nanoparticles. Nanomaterials 2019;9:430.
[47] Ditta A, Khan MA, Junaid M, Khalil RMA, Warsi MF. Structural, magnetic, and spectral properties of Gd and Dy co-doped dielectrically modified Co-Ni ($Ni_{0.4}Co_{0.6}Fe_2O_4$) ferrites. Phys B Condens Matter 2017;507:27–34.
[48] Stoner EC, Wohlfarth EP. A mechanism of magnetic hysteresis in heterogeneous alloys. Philos Trans R Soc London Ser A, Math Phys Sci 1948;240:599–642.
[49] Korkmaz ADD, Güner S, Slimani Y, Gungunes H, Amir MM, Manikandan A, et al. Microstructural, optical, and magnetic properties of vanadium-substituted nickel spinel nanoferrites. J Supercond Nov Magn 2019;32:1057–65.
[50] Almessiere MA, Slimani Y, Baykal A. Impact of Nd-Zn co-substitution on microstructure and magnetic properties of $SrFe_{12}O_{19}$ nanohexaferrite. Ceram Int 2019;45:963–9.
[51] Almessiere MAA, Slimani Y, El Sayed HSS, Baykal A. Morphology, and magnetic traits of strontium nanohexaferrites: effects of manganese/yttrium co-substitution. J Rare Earths 2019;37:732–40.
[52] Almessiere MA, Slimani Y, Ali S, Baykal A, Ercan I, Sozeri H. Nd^{3+} ion-substituted $Co_{1-2x}Ni_xMn_xFe_{2-y}Nd_yO_4$ nanoparticles: structural, morphological, and magnetic investigations. J Inorg Organomet Polym Mater 2019;29:783–91.
[53] Almessiere MA, Slimani Y, Güner S, Nawaz M, Baykal A, Aldakheel F, et al. Magnetic and structural characterization of Nb^{3+}-substituted $CoFe_2O_4$ nanoparticles. Ceram Int 2019;45:8222–32.
[54] Akhtar MN, Khan MA. Effect of rare earth doping on the structural and magnetic features of nanocrystalline spinel ferrites prepared via sol gel route. J Magn Magn Mater 2018;460:268–77.
[55] Slimani Y, Almessiere MA, Güner S, Tashkandi NA, Baykal A, Sarac MF, et al. Calcination effect on the magneto-optical properties of vanadium substituted $NiFe_2O_4$ nanoferrites. J Mater Sci Mater Electron 2019;30:9143–54.
[56] Almessiere MAA, Slimani Y, Korkmaz ADD, Taskhandi N, Sertkol M, Baykal A, et al. Sonochemical synthesis of Eu^{3+} substituted $CoFe_2O_4$ nanoparticles and their structural, optical, and magnetic properties. Ultrason Sonochem 2019;58:104621.
[57] Kokare K, Jadhav NA, Kumar Y, Jadhav KM, Rathod SM. Effect of Nd^{3+} doping on structural and magnetic properties of $Ni_{0.5}Co_{0.5}Fe_2O_4$ nanocrystalline ferrites synthesized by sol-gel auto combustion method. J Alloys Compd 2018;748:1053–61.
[58] Slimani Y, Almessiere MA, Korkmaz AD, Guner S, Güngüneş H, Sertkol M, et al. $Ni_{0.4}Cu_{0.2}Zn_{0.4}Tb_xFe_{2-x}O_4$ nanospinel ferrites: ultrasonic synthesis and physical properties, Ultrason. Sonochem 2019;59:104757.
[59] Alone ST, Shirsath SE, Kadam RH, Jadhav KM. Chemical synthesis, structural and magnetic properties of nano-structured Co-Zn-Fe-Cr ferrite. J Alloys Compd 2011;509:5055–60.
[60] Alahmari F, Almessiere MA, Slimani Y, Güngüneş H, Shirsath SE, Akhtar S, et al. Synthesis, and characterization of electrospun $Ni_{0.5}Co_{0.5-x}Cd_xNd_{0.02}Fe_{1.78}O_4$ nanofibers. Nano-Struct Nano-Objects 2020;24:100542.
[61] Zaquine I, Benazizi H, Mage JC. Ferrite thin films for microwave applications. J Appl Phys 1988;64:5822–4.
[62] Vinosha PAA, Manikandan A, Ragu R, Dinesh A, Thanrasu K, Slimani Y, et al. Impact of nickel substitution on structure, magneto-optical, electrical, and acoustical properties of cobalt ferrite nanoparticles. J Alloys Compd 2020:157517.
[63] Almessiere MA, Slimani Y, Shirsath SE, Wudil YS, Baykal A, Ercan I. Customized magnetic properties of $(Mn_{0.5}Zn_{0.5})[Eu_xNd_xFe_{2-2x}]O_4$ nanospinel ferrites synthesized via ultrasonic irradiation approach. Results Phys 2020;19:103350.
[64] Shirsath SE, Mane ML, Yasukawa Y, Liu X, Morisako A. Chemical tuning of structure formation and combustion process in $CoDy_{0.1}Fe_{1.9}O_4$ nanoparticles: influence@pH. J Nanoparticle Res 2013;15:1–13.
[65] Almessiere MA, Slimani Y, Gungunes H, Manikandan A, Baykal A. Investigation of the effects of Tm^{3+} on the structural, microstructural, optical, and magnetic properties of Sr hexaferrites. Results Phys 2019;13:102166.
[66] Almessiere MA, Slimani Y, Kurtan U, Guner S, Sertkol M, Shirsath SE, et al. Structural, magnetic, optical properties and cation distribution of nanosized $Co_{0.7}Zn_{0.3}Tm_xFe_{2-x}O_4$ ($0.0 \leq x \leq 0.04$) spinel ferrites synthesized by ultrasonic irradiation. Ultrason Sonochem 2019;58:104638.
[67] Sadaqat A, Almessiere M, Slimani Y, Guner S, Sertkol M, Albetran H, et al. Structural, optical, and magnetic properties of Tb^{3+} substituted Co nanoferrites prepared via sonochemical approach. Ceram Int 2019;45:22538–46.
[68] Hassanzadeh-Tabrizi SA, Behbahanian S, Amighian J. Synthesis and magnetic properties of $NiF_{e2-x}Sm_xO_4$ nanopowder. J Magn Magn Mater 2016;410:242–7.
[69] Almessiere MAA, Slimani Y, Korkmaz ADD, Sertkol M, Baykal A, Ercan I, et al. Sonochemical synthesis of $CoFe_{2-x}Nd_xO_4$ nanoparticles: structural, optical, and magnetic investigation. J Supercond Nov Magn 2019;32:3837–44.
[70] Almessiere MA, Slimani Y, Baykal A. Synthesis, and characterization of $Co_{1-2x}Ni_xMn_xCe_yFe_{2-y}O_4$ nanoparticles. J Rare Earths 2020;38:188–94.
[71] Iorgu AI, Maxim F, Matei C, Ferreira LP, Ferreira P, Cruz MM, et al. Fast synthesis of rare-earth (Pr^{3+}, Sm^{3+}, Eu^{3+} and Gd^{3+}) doped bismuth ferrite powders with enhanced magnetic properties. J Alloys Compd 2015;629:62–8.
[72] Slimani Y, Unal B, Almessiere MA, Korkmaz AD, Shirsath SE, Yasin G, et al. Investigation of structural and physical properties of Eu^{3+} ions substituted $Ni_{0.4}Cu_{0.2}Zn_{0.4}Fe_2O_4$ spinel ferrite nanoparticles prepared via sonochemical approach. Results Phys 2020;17:103061.